Machining simulation of Ti6Al4V using coupled Eulerian-Lagrangian approach and a constitutive model considering the state of stress

Xiang Xu [a,b], José Outeiro [a,*], Jun Zhang [b,*], Binbin Xu [b], Wanhua Zhao [b], Viktor Astakhov [c]

[a] Arts et Metiers Institute of Technology, LaBoMaP, HESAM University, Rue Porte de Paris, 71250 Cluny, France
[b] State Key Laboratory for Manufacturing Systems Engineering, Xi'an Jiaotong University, Xi'an, Shaanxi, 710054, China
[c] Production Service Management Inc. (PMSi), Saline, MI, USA

ARTICLE INFO

Keywords:
Coupled Eulerian-Lagrangian
Lagrangian
State of stress
Constitutive model
Machining
Ti6Al4V

ABSTRACT

The accuracy of a machining model depends on the capability of this model to describe the physical phenomena associated to the real machining system. This includes the material constitutive model and the approach used to describe the field flow of the material in cutting. In this paper, a model of high speed machining (HSM) of Ti6Al4V titanium alloy is developed. This cutting model includes the proposed constitutive model considering the influence of strain hardening, strain-rate, temperature, and state of stress (e.g., stress triaxiality and Lode parameter) in the material plasticity and damage. Finite Element Method (FEM) using Coupled Eulerian-Lagrangian (CEL) approach is used to simulate the cutting model. A sensitivity analysis of the influence of the mesh topography on the chip geometry and cutting force is performed resulting in the determination of the optimal element size and element orientation. Simulation results obtained using the CEL approach are compared with those obtained using the Lagrangian one. Moreover, simulated cutting force and chip geometry obtained using the proposed constitutive model are compared with those obtained using the Johnson-Cook (J-C) model, and experimental data. Both chip geometry and cutting force predicted by the proposed constitutive model is closer to the experimental one than the J-C constitutive model. The CEL approach combined with the proposed constitutive model can simulate material side flow, which results in a larger width of chip compared to the width of cut, and in the formation of lateral burr on the workpiece. It also permits simulating the cyclic variation of the plastic strain and topography of the machined surface along the cutting direction, observed experimentally.

1. Introduction

New advances in the modelling of the machining process are of great significance to improve component performance, life in service, and their manufacturing efficiency. Considering the high cost and time consumption of the experimental machining tests and the difficulties to obtain some data from these tests (e.g. strain, cutting temperature, and residual stress distributions), the application

* Corresponding author.
E-mail addresses: jose.outeiro@ensam.eu (J. Outeiro), junzhang@xjtu.edu.cn (J. Zhang).

https://doi.org/10.1016/j.simpat.2021.102312

of the numerical simulation to the machining process has outstanding advantages. Developing a model that can predict the outcomes of the machining process accurately is full of challenges and many efforts have been made to reach this goal. Every cutting model is established for its particular research purposes, such as tool wear [1], forces [2], and surface integrity [3], including microstructure evolution [4]. Simulation results are highly dependent on the input data, although the use of the same input data yields different results when different cutting models are used [5]. Meshing, constitutive material model, contact model, boundary conditions, and so on directly affect the adequacy and accuracy of the predicted results [6]. It is generally accepted amongst researchers dealing with modelling of machining operations that problems with a relevant constitutive model to describe the mechanical behavior of the work material in cutting and the control of the mesh distortion in the Finite Element (FE) simulations still need to be addressed properly [7, 8].

As far as the simulation methods applied to the machining process are concerned, the traditional Lagrangian approach is widely adopted, in which element deletion and mesh distortion control are required. The critical issue of this approach is the element distortion due to the severe plastic deformation induced by cutting. To overcome this issue, several meshless methods are developed, such as Smoothed Particle Hydrodynamics (SPH) [9] and Discrete Element Method (DEM) [10]. However, the convergence of these meshless methods is quite difficult and their accuracy strongly depends on the initial arrangement of particles [11]. Therefore, to solve the problem of the element distortion associated with the Lagrangian approach, three methods or hybrid approaches are developed: Lagrangian with remeshing, Arbitrary Lagrangian Eulerian (ALE), and Coupled Eulerian Lagrangian (CEL). The major problem of the remeshing approach is the accumulation of calculation errors caused by nodes migration and data interpolation from one mesh to another [1]. Taking the advantages of both Lagrangian and Eulerian approaches, ALE describes the chip formation as a material flow around the tool cutting edge, which does not require any element deletion or fracture criterion to separate the material from the workpiece to form the chip. ALE approach may be used for simulating continuous chip formation [13,14], but it is unable to simulate serrated chips, like those observed in the machining of difficult-to-cut materials. Zhang et al. [5] conducted orthogonal cutting simulations using Lagrangian, ALE, and CEL approaches. The simulation results show that the problems of element distortion and material loss are avoided by using ALE and CEL approaches, but the formation of serrated chips cannot be simulated if the damage material model is not used. The use of the CEL approach can help to avoid the mesh distortion, and the stable time increment is not reduced when compared to the ALE one. Ducobu et al. [15] proposed a cutting model of Ti6Al4V using the CEL approach, which considers the workpiece as an Eulerian region and the cutting tool as a Lagrangian one. They analyzed the effect of the element size and shape on the simulation results. However, they could only simulate continuous chips, partially due to the low cutting speed (30 m/min) used in their machining simulations [16,17]. Later, Shuang et al. [18] successfully simulated a serrated chip in machining of Ti6AL4V under extremely high cutting speed of 1200 m/min. The results of their modelling show that, for a cutting speed of 60 m/min, the simulated chip is continuous, whereas the serrated chip was obtained experimentally [19]. Moreover, it is worth noting that the simulated plastic strain in the shear band of the chip is extremely high compared to the strain at fracture of the Ti6AL4V obtained in the material testing [20].

The numerical simulation of the machining process is highly dependent on the constitutive model, which describes the material behavior under various loading conditions found in metal cutting [8]. Johnson-Cook (J-C) constitutive model is often applied in the simulation of manufacturing processes including machining [21]. The problem is that for the same material, a number of different J-C plasticity model coefficients can be found in the literature [22]. A sensitivity analysis of these coefficients shows that they have a significant influence on the simulation results. Often researchers select and test several sets of J-C model coefficients to determine which is the best set to use in their particular case [22,23]. Several studies have also shown that the J-C constitutive model is not suitable to represent the mechanical behavior of the work material in machining adequately [8]. Therefore, the J-C model has been modified or new constitutive models have been proposed to achieve an accurate description of the mechanical behavior of the work material in machining [24–26]. To address the difficulty of the J-C plasticity model to capture the serrated chip formation, Calamaz et al. [24] proposed a constitutive model (called the TANH model) to better predict serrated chips, which considers the effect of strain softening on the flow stress. Sima and Özel [25] made some improvements to this model to better control strain softening behavior. However, the accuracy of this model is only verified through orthogonal cutting tests rather than mechanical tests. Except the above phenomenological models, several physic-based constitutive models have been developed to simulate the cutting process. Sadeghifar et al. [27] developed a cutting model using the Johnson-Mehl-Avrami-Kolmogorov (JMAK) constitutive model to study the effect of cutting parameters on grain size alterations induced by machining of Ti6Al4V alloy. Estrin and Kim [28] proposed a dislocation density based constitutive model that has been applied in the cutting simulation of pure copper and pure aluminum [29]. Imbrogno et al. [30] proposed a material microstructural-based constitutive model based on dislocation density and grain size considering the long-range and short-range contributions to simulate the serrated chip formation in the machining of Waspaloy. The basic problems of such material microstructural-based constitutive models are: (1) great difficulties to obtain the microstructure properties of a given work material to determine the constitutive model coefficients; (2) assure the constancy of the microstructural properties over various regions of the material.

The formation of cracks in chip formation (tearing) and cyclic nature of chip formation were recognized by the most noticeable classical work in metal cutting by Time [31], Nicolson [32], Taylor [33], Okoshi and Fucui [34]. In modern terminology, it is considered as cyclic fracture in chip formation [7,35–37]. Childs et al. [38] proposed a combined flow stress and failure model to simulate the serrated chip formation process of Ti6Al4V alloy over a wide cutting speed range, which improved the prediction accuracy of FE cutting model. Therefore, work material damage and fracture as state of stress dependent phenomena must be considered when modelling material behavior. Bai and Wierzbicki [12,39] proposed a constitutive model considering the effect of the state of stress (stress triaxiality and Lode parameter) on the material plasticity and damage. Wang et al. [37,40] found that the stress triaxiality in the first deformation zone (FDZ) gradually increased from negative near the tool cutting edge to positive in the chip free surface,

which has a great influence on the formation of serrated chips and fracture strain distribution. Therefore, a constitutive model considering the effect of the state of stress is essential for describing the mechanical behavior of the work material in cutting as its use greatly increases the prediction accuracy. However, only a few constitutive models used in metal cutting considers the state of stress. Cheng et al. [20] proposed a constitutive model that considers the effect of strain hardening, strain-rate, and the state of stress on the mechanical behavior of Ti6Al4V alloy. The accuracy of this model is verified for different samples geometry and loading conditions (thus different state of stress), by comparing the predicted force-displacement curves obtained using this constitutive model and the experimental curves. This accuracy is not confirmed using the J-C model.

Although modeling and simulation using two-dimensional (2D) Finite Element Method (FEM) have significantly improved and helped to understand the fundamental mechanisms of the cutting process during the past decades [6], it is based on the assumption of the plane strain conditions. Therefore, it cannot be used to describe the cutting process mechanics in real 3D machining operations, such as turning, drilling, and milling. As a result, three-dimensional (3D) cutting models of those machining operations have been developed to predict forces, temperatures, tool wear, and surface integrity [41–44]. Attanasio et al. [45] developed a 3D model to simulate tool wear in drilling of Inconel by updating the geometry of the worn tool using a new algorithm considering the tool wear rate. Ying et al. [46] established a 3D model of the milling of Ti-6Al-4V titanium alloy to predict the cutting force, cutting temperature, and residual stresses. Liu et al. [47] developed a 3D model of turning using a new designed micro-textured cutting tool to investigate its cutting performance. Outeiro et al. [48] developed a 3D model of turning of Inconel 178 and AISI 316L stainless steel to investigate the thermomechanical phenomena in machining these two difficult-to-cut materials, and correlate these phenomena with the residual stresses in the machined surfaces. It is worth noting that none of these 3D models are able to simulate serrated chips, and thus they could not reproduce the cyclic variation of the plastic strain and topography of the machined surface observed experimentally [49]. Therefore, there are a need to develop a model of cutting to accurate reproduce the cyclic nature of the chip formation process, and its influence on the thermomechanical phenomena and surface integrity.

This paper proposes a new procedure to simulate the serrated chip formation, and consequently the cyclic variation of the forces and surface integrity parameters in high speed machining (HSM) of Ti6Al4V titanium alloy. This procedure is based on the CEL approach combined with a constitutive model considering the strain hardening, strain-rate, temperature, and state of stress (e.g., stress triaxiality and Lode parameter) in the material plasticity (flow stress) and damage.

The paper starts by determining the suitable mesh geometry for the simulations using the CEL approach, including the element size and the element orientations/shape. Then, CEL approach is used to investigate the state of stress and fracture strain in the FDZ particularly related to the cutting speed. The results obtained using the proposed constitutive model and CEL approach are compared with those obtained using the Lagrangian one using the same constitutive model. To evaluate the accuracy of the proposed constitutive model to predict the metal cutting outcomes (forces, chip geometry, etc.), the simulation results obtained using this constitutive model are compared with the results obtained using the J-C model, and with those obtained experimentally. Finally, material side flow, and the cyclic variation of the surface topography and plastic strain along the cutting direction are investigated using the cutting model based on the CEL approach.

2. Modelling and simulation of HSM

2.1. Description of the orthogonal cutting models

Orthogonal cutting models of HSM of Ti6Al4V titanium alloy are developed and simulated by FEM using the CEL and Lagrangian approaches, available in ABAQUS/Explicit software.

Fig. 1 shows the orthogonal cutting model using the CEL approach, which can only be used for 3D simulations [50]. This 3D model has an extremely small width of cut (only 4 μm) when compared to the workpiece length and height (hereby called CEL1 model). In this

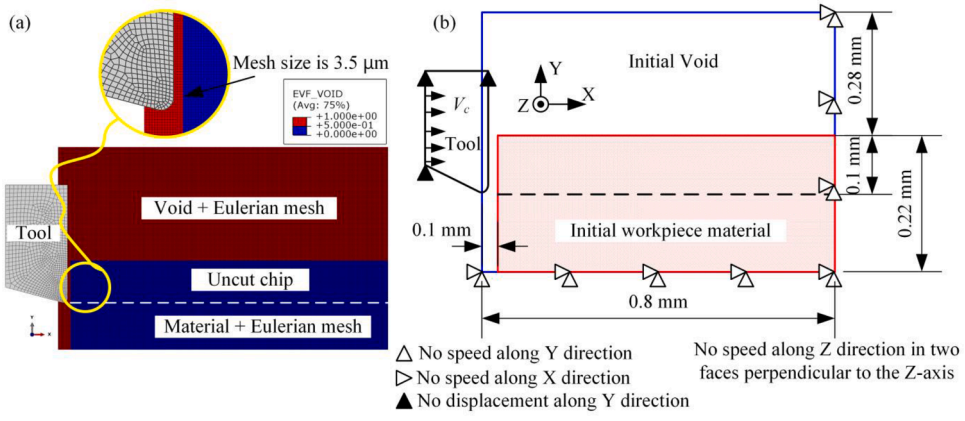

Fig. 1. Orthogonal cutting model having an extremely small width of cut (only 4 μm) using the CEL approach (CEL1 model): (a) mesh and (b) boundary conditions.

model, the tool is described by the Lagrangian approach while the workpiece is described by the Eulerian one. Eulerian Volume Fraction (EVF) plays an important role in CEL simulations, so it will be tracked to measure the ratio of material inside the element. Fig. 1a shows the initial state of the model, where the blue colored of elements means that they are filled with material (EVF = 1), while the red colored elements are empty (EVF ≈ 0).

Because the displacement of the Eulerian element cannot be constrained, a zero-velocity boundary condition will be used. As shown in Fig. 1b, the workpiece movement is constrained in the vertical (the Y-direction) and horizontal (the X-direction) by applying the zero-velocity boundary condition at the bottom and right-side surfaces of the model. The tool is constrained to have zero displacements along the Y-direction and the velocity equal to the cutting speed in the positive X-direction. To avoid the material flow out of the Eulerian region, the zero velocity boundary condition is applied in front and back surfaces of the model in the Z-direction. The Lagrangian region (tool) is in contact with Eulerian one (workpiece) inside the Eulerian mesh [15,50].

The workpiece, including both void and material regions, is meshed using the 8-node thermo-mechanical coupled linear Eulerian brick elements (EC3D8RT) with reduced integration and hourglass control features. The tool is meshed as the 8-node linear thermo-mechanical coupled brick elements (C3D8RT). The cutting time and cutting length need to be determined carefully to make sure that the material flow is all inside the Eulerian mesh boundaries for all the cutting conditions.

The element size and element orientation of the workpiece directly determine the convergence of the calculation process and have a great impact on the results. To balance the accuracy and efficiency of the simulation, the effect of the element size and element orientation angle on simulation results will be investigated. Besides that, the element size of the tool in the tool-chip contact zone is chosen to be similar to the workpiece. Initial homogeneous temperature distribution of 20°C is applied to the workpiece and tool.

Since only 3D models can be developed using CEL approach [50], the calculation time is higher compared to the traditional 2D models using Lagrangian or ALE approaches. For this reason, the previous orthogonal cutting model using CEL approach uses an extremely small width of cut (only 4 μm) to minimize this calculation time. However, very small width of cut does not allow the material to flow freely in the Z-direction, thus it cannot reproduce the lateral burr formation and a larger chip width used in orthogonal cutting tests of several work materials [51,52]. Therefore, a second 3D orthogonal cutting model with a larger width of cut equal to 3 mm is proposed (hereby called CEL2 model). To reduce the computation time, a symmetry plane perpendicular to the Z-direction is applied, thus the width of the workpiece is equal to 1.5 mm. This model is shown in Fig. 2, where a volume of void having 0.5 mm of width is used in the back side of the workpiece to allow material side flow freely in the Z-direction. The workpiece movement is constrained in the vertical (Y- direction) and horizontal (X-direction) by applying a zero-velocity boundary condition at the bottom and right surfaces of the model. The workpiece including the void and material regions is meshed using the 8-node thermo-mechanical coupled linear Eulerian brick elements (EC3D8RT) with reduced integration and hourglass control features. The tool is meshed as the 8-node linear thermo-mechanical coupled brick elements (C3D8RT). According to Liu et al. [53], the stress and strain distributions are uniform in the interior of the chip/machined part, while in the border (the interface between the material and the void in the CEL model) these distributions change significantly. Pednekar et al. [54] show that, when the ratio between the width of cut and the uncut chip thickness reaches a critical value of 20, more than 90% of the chip width can undergo plane strain conditions. The model shown in Fig. 2 has a ratio of 30, so most of the workpiece is in plane strain conditions. Therefore, a coarser element size in the interior of the workpiece does not reduce the simulation accuracy and increases the calculation efficiency. The element size of this model in the XY plane is 3.5 μm (the same as in the CEL1 model), while this size in Z-direction ranges from 3.5 μm to 100 μm (finer mesh near the interface between the material and the void, and coarser mesh in the other zones).

Finally, a 2D model of orthogonal cutting using the Lagrangian approach is also developed (hereby called LAG model), as shown in

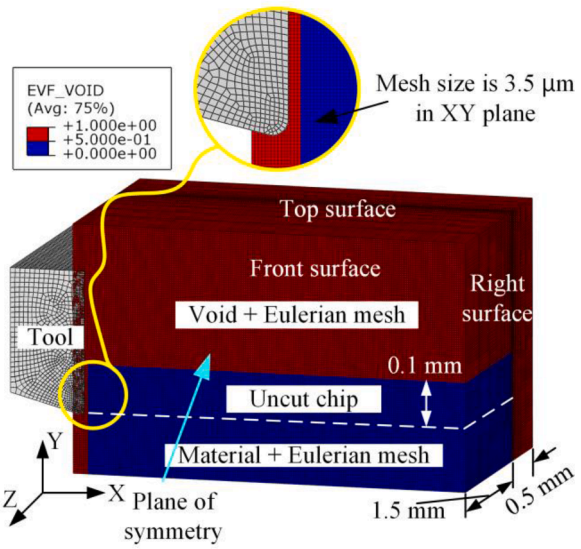

Fig. 2. Orthogonal cutting model having a larger width of cut (3 mm) using the CEL approach (CEL2 model).

Fig. 3. This figure shows the workpiece composed by the uncut chip layer, sacrificial layer, and remaining part of the workpiece. The workpiece is meshed using the planar quadrilateral continuum elements (CPE4RT) with four-node, plane strain, with reduced integration features suitable for large deformation analysis. The tool is meshed as three-node linear displacement and temperature elements (CPE3T) with plane strain features. The element sizes in the uncut chip and sacrificial layers are determined by a sensitivity analysis on the influence of this parameter in the forces and chip geometry. The obtained values are 5 μm and 2.5 μm, respectively. The bottom of the workpiece is fixed and the tool is moving along the X-direction only, from right to left at a constant cutting speed. Besides that, element size of the tool in the tool-chip contact zone is set less than that of the workpiece.

The geometry of finite elements used in the CEL simulations (element size and its orientation/shape) was determined based on the sensitive analysis of the influence of this geometry on the forces and chip geometry. This analysis is presented and discussed in section 4.1. Similar study was already conducted by the authors using the Lagrangian approach [19].

Cutting conditions, contact model, material properties and constitutive model are the same for the three models. Four values of the cutting speed were used: 50, 125, 250 and 500 m/min. The uncut chip thickness and width of cut are set constant equal to 0.1 mm and 3 mm, respectively. The physical, thermal, and elastic properties of the work material are shown in Table 1. Uncoated cemented carbide (WC-Co) cutting tools are used, and the corresponding physical, thermal, and elastic properties are given in Table 1. Tool geometry is represented by the rake angle of 0°, a clearance angle of 15°, and cutting edge radius of 10 μm. In machining practice, the maximum recommended cutting speed for machining of Ti6Al4V titanium alloy using a cemented carbide tool is about 120 m/min.

For higher cutting speed such as those speeds used in this research work, polycrystalline diamond (PCD) is the suitable tool material for machining of Ti6Al4V titanium alloy. However, uncoated cemented carbide tools are used in the present study, keeping the cutting length extremely short and one cutting edge per tests, to avoid tool wear effects on the results.

As far as the tool-chip contact is concerned, Zorev's model [58] is used, which considers two contact regions: i) a plastic region near the cutting edge, with a limit shear stress equal to the yield shear stress of the chip material, and; ii) a sliding region near the end of the tool-chip contact, where the tangential contact stress τ_f is proportional to the normal stress σ_n at the tool-chip interface. Zorev's model can be represented by the following equation:

$$\tau_f = \begin{cases} \tau_Y & if \quad \mu\sigma_n \geq \tau_Y \quad (plastic \text{ region}) \\ \mu\sigma_n & if \quad \mu\sigma_n < \tau_Y \quad (sliding \text{ region}) \end{cases} \tag{1}$$

where μ is the coulomb's friction coefficient, and τ_Y is the yield shear stress of the work material. Yield shear stress can be correlated with the yield stress using for instance the Von Mises criterion, thus $\tau_Y = \sigma_Y / \sqrt{3}$ under various state of stress. The friction coefficient depends on the contact conditions, including the temperature, contact pressure, and sliding speed. Courbon et al. [59] showed that the friction coefficient between the Ti6Al4V alloy and the cemented carbide tool depends mainly on the sliding speed, and can be given by the following equation:

$$\mu = 0.48 \times V_s^{-0.1904} \tag{2}$$

where V_s is the sliding speed of the chip over the tool. The thermal conductance in the tool-workpiece contact interface is equal to 1000 kW/(m^{2}K) according to Sima and Ozel [25].

2.2. Definition of state of stress

The proposed constitutive model considers the effect of state of stress on both material plasticity and damage. This state of stress is characterized by the stress triaxiality and the Lode parameter [12]. Three invariants of the stress tensor are defined by:

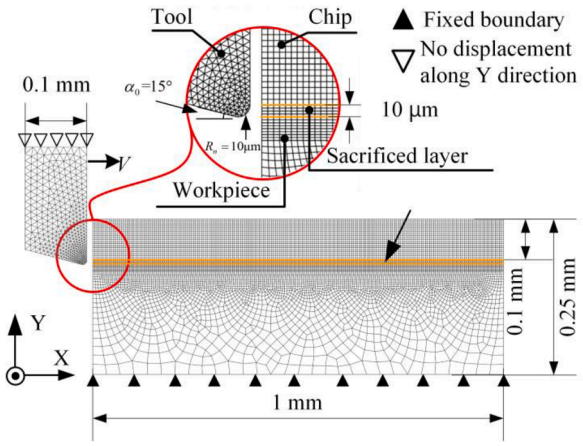

Fig. 3. Mesh and boundary conditions of 2D orthogonal cutting model using Lagrangian approach (LAG model).

Table 1

Physical, thermal, and elastic properties of the work and tool materials [24,55–57].

Material	Density (kg m^{-3})	Elastic modulus (GPa)	Poisson's ratio	Specific heat (J $kg^{-1}K^{-1}$)	Thermal conductivity (W $m^{-1}K^{-1}$)	Expansion (K^{-1})
WC-Co	11900	534	0.22	400	50	-
Ti6Al4V	4430	109	0.34	611	6.8	1E-5

$$p = -\sigma_m = -\frac{1}{3}(\sigma_1 + \sigma_2 + \sigma_3) \tag{3}$$

$$q = \overline{\sigma} = \sqrt{\frac{3}{2}\mathbf{S} : \mathbf{S}} = \sqrt{\frac{1}{2}[(\sigma_1 - \sigma_2)^2 + (\sigma_2 - \sigma_3)^2 + (\sigma_3 - \sigma_1)^2]} \tag{4}$$

$$r = \left(\frac{9}{2}\mathbf{S} : \mathbf{S} : \mathbf{S}\right)^{1/3} = \left[\frac{27}{2}(\sigma_1 - \sigma_m)(\sigma_2 - \sigma_m)(\sigma_3 - \sigma_m)\right]^{1/3} \tag{5}$$

where σ_1, σ_2 and σ_3 denote the three principal stresses, σ_m is the mean principal stress, **S** is the deviatoric stress tensor. Stress triaxiality η and Lode parameter are defined as follows:

$$\eta = \frac{-p}{q} = \frac{\sigma_m}{\overline{\sigma}} \tag{6}$$

$$\begin{cases} \xi = \left(\dfrac{r}{q}\right)^3 = \cos(3\theta) \\ \overline{\theta} = 1 - \dfrac{6\theta}{\pi} = 1 - \dfrac{2}{\pi}\arccos\xi \end{cases} \tag{7}$$

where ξ and $\overline{\theta}$ are the normalized third deviatoric stress invariant and the normalized Lode angle (also called Lode parameter). The range of $\overline{\theta}$ is between [-1, 1].

2.3. Proposed constitutive model

An accurate and reliable constitutive model is very important to describe the mechanical response of the work material in machining. The J-C constitutive model [21] is widely used to describe the mechanical behavior of the work under different strain-rates and temperatures but is not accurate for relatively small strains and complex state of stress. Therefore, a constitutive model considering the effect of strain hardening, thermal softening, strain rate, and state of stress are proposed in this study. This model is an extension of the constitutive model of Cheng et al. [20] by including the effect of the temperature on the material plasticity and damage.

2.3.1. Plasticity

The plasticity part of the proposed model is given by equation (8), where the strain hardening, strain rate, and temperature terms are based on the Dos Santos et al. [60] and Johnson and Cook [21] models, respectively. As far as the state of stress term is concerned, it is based on the Bai and Wierzbicki [12] and Cheng et al. [20] model.

$$\begin{aligned} \overline{\sigma} = (A + m\varepsilon^n)\left[B + C\ln\left(E + \frac{\dot{\varepsilon}}{\dot{\varepsilon}_0}\right)\right]\left[1 - \left(\frac{T - T_r}{T_m - T_r}\right)^h\right] \\ \times[1 - c_\eta(\eta - \eta_0)]\left[c_\theta^s + \left(c_\theta^{ax} - c_\theta^s\right)\left(\gamma - \frac{\gamma^{a+1}}{a+1}\right)\right] \end{aligned} \tag{8}$$

$$\gamma = 6.464[\sec(\overline{\theta}\pi/6) - 1] \tag{9}$$

$$c_\theta^{ax} = \begin{cases} c_\theta^t & \text{when } \overline{\theta} > 0 \\ c_\theta^c & \text{when } \overline{\theta} \le 0 \end{cases} \tag{10}$$

Table 2

Coefficients of the plasticity part of the proposed constitutive model of Ti6Al4V alloy taken from the work of Cheng et al [20].

Coefficient	A (MPa)	m (MPa)	n	B	C	E	$\dot{\varepsilon}_0$ (s^{-1})	T_r (°C)
Value	812.1	625.7	0.176	0.4	0.073	3949	0.05	20
Coefficient	T_m (°C)	h	η_0	c_η	c_θ^s	c_θ^t	c_θ^c	a
Value	1620	1	-1/3	0.212	0.795	1.061	1	4

In these equations: i) $\bar{\sigma}$ is the equivalent stress; ii) ε and $\dot{\varepsilon}$ are the equivalent plastic strain and strain rate, respectively; iii) T is temperature; iv) η is the stress triaxiality; v) η_0 is the reference stress triaxiality; vi) $\dot{\varepsilon}_0$ is the reference strain rate; and vii) T_r and T_m are the room and melting temperatures, respectively, A, m, n, B, C, E, and h are the coefficients of the plasticity model associated to the strain hardening, strain rate, and temperature terms, while c_η, $c_{\bar{\theta}}^s$, $c_{\bar{\theta}}^c$, $c_{\bar{\theta}}^t$ and a are the coefficients associated to the state of stress (stress triaxiality and Lode parameter) term. The values of these coefficients are given in Table 2, which are determined by Cheng et.al [20]. Fig. 4 shows the stress-strain curves obtained by plotting the proposed constitutive model given by equations 8–10 and the coefficients presented in Table 2, for the work material in FDZ with a temperature of 350 °C, strain rate of 10^5 s^{-1}, and several values of stress triaxiality and Lode parameter. $\bar{\varepsilon}_0^{pl}$ is the strain at damage initiation, calculated using Eq. 12 that will be described later, and the coefficients presented in Table 3. As can be seen in this figure, the stress-strain curves are affected by the stress triaxiality and the Lode parameter.

2.3.2. Damage initiation and evolution

To describe the material behavior in machining properly, the constitutive model must also consider material failure. This permits more realistic modeling of the chip formation (chip serration and the localized shear strain in the shear bands) in the machining of Ti6Al4V [61]. In this study, an energy-based ductile fracture criterion is adopted, which is composed of two stages, i.e. damage initiation and damage evolution [20]. The damage initiation is described by the variable w defined as:

$$w = \sum \frac{\Delta \bar{\varepsilon}^{pl}}{\bar{\varepsilon}^{pl}{}_0} \tag{11}$$

where $\bar{\varepsilon}^{pl}{}_0$ is the equivalent plastic strain at damage initiation and $\Delta\bar{\varepsilon}^{pl}$ is an increment of the equivalent plastic strain. As shown in Fig. 5, w increases continuously with plastic deformation, and when it is equal to 1, damage evolution is activated. $\bar{\varepsilon}^{pl}{}_0$ can be calculated by Eq. (12), based on Bai and Wierzbicki [12] and Johnson-Cook [62] constitutive models depending upon the stress triaxiality, Lode parameter, strain rate, and temperature.

$$\bar{\varepsilon}^{pl}{}_0 = \left\{ \left[\frac{1}{2}\left(D_1 e^{-D_2\eta} + D_5 e^{-D6\eta}\right) - D_3 e^{-D_4\eta} \right] \bar{\theta}^2 + \frac{1}{2}\left(D_1 e^{-D_2\eta} - D_5 e^{-D_6\eta}\right)\bar{\theta} + D_3 e^{-D_4\eta} \right\} \times \left[1 + D_7 \ln\left(\frac{\dot{\varepsilon}}{\dot{\varepsilon}_0}\right) \right] \left(1 + D_8 \frac{T - T_r}{T_m - T_r} \right) \tag{12}$$

In this equation, D_1 to D_6 are coefficients as in the Bai and Wierzbicki model, while D_7 and D_8 are as in the J-C one. These coefficients are determined by Cheng et al. [20] and given in Table 3. Moreover, the damage initiation point is calculated and given in Fig. 4 according to the above damage initiation model, which reveals that the damage initiation starts at different equivalent strains depending upon the state of stress.

The equivalent strain at damage initiation $\bar{\varepsilon}^{pl}{}_0$ as a function of the state of stress $(\eta,\ \bar{\theta})$ for the Ti6Al4V alloy in FDZ at temperature of 350 °C and a strain rate of 10^5 s^{-1} are calculated and presented in Fig. 6. As can be seen, when the stress triaxiality is 1 and the Lode parameter is 0, the minimum of the plastic strain at damage initiation is the case obtained. Decreasing the Lode parameter from 0 to -1 or increasing it from 0 to 1 results in increasing the plastic strain at damage initiation. However, the plastic strain at damage initiation decreases as the stress triaxiality increases from -1 to 1.

In Fig. 5, $\bar{\varepsilon}^{pl}{}_f$ is the plastic strain at the point where the material has lost all its stiffness and dissipated all the fracture energy.

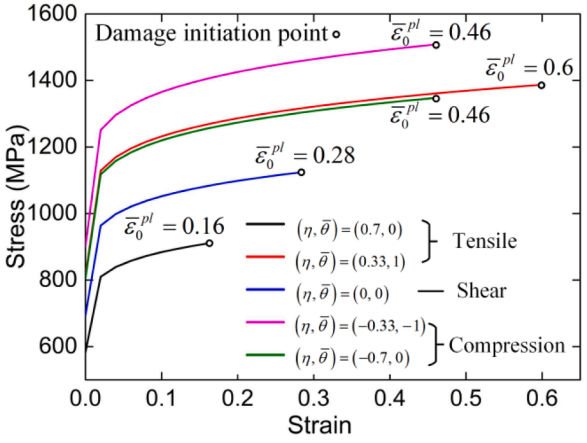

Fig. 4. Stress-strain curves of the proposed constitutive model of Ti6AL4V titanium alloy in the FDZ (temperature = 350 °C, strain rate = 10^5 s^{-1}, and several values of stress triaxiality and Lode parameter).

Table 3

Coefficients of the damage initiation of Ti6Al4V alloy taken from the work of Cheng et al [20].

D_1	D_2	D_3	D_4	D_5	D_6	D_7	D_8
0.694	0.608	0.263	0.734	0.43	0.04	-0.028	3.87

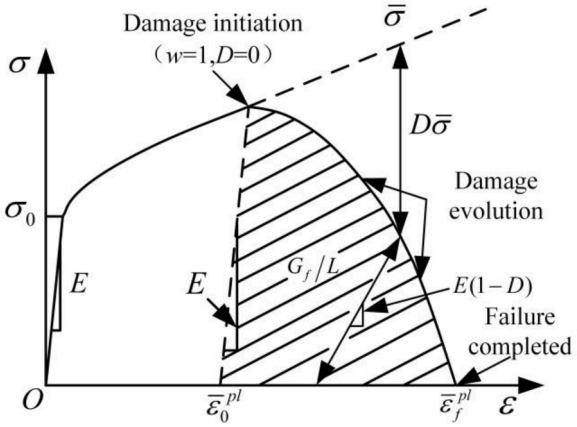

Fig. 5. Schematic representation of the stress-strain curve showing the material damage.

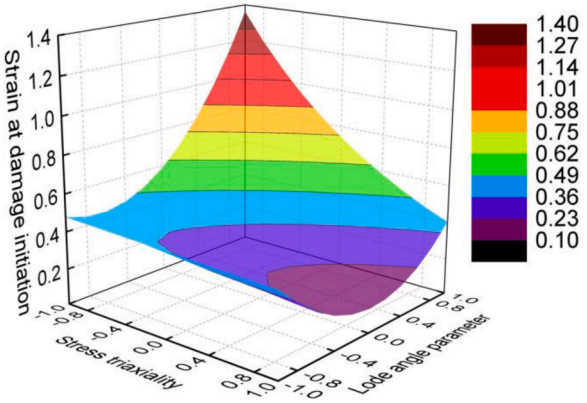

Fig. 6. Strain at damage initiation for the Ti6Al4V alloy in FDZ in function of the stress triaxiality and Lode parameter (temperature of 350 °C and a strain rate of 10^5 s^{-1}).

Therefore, $\bar{\varepsilon}^{pl}{}_f$ can be calculated using the following equation:

$$G_f = \int_{\bar{\varepsilon}_0^{pl}}^{\bar{\varepsilon}_f^{pl}} L\sigma_y d\bar{\varepsilon}^{pl} \tag{13}$$

where G_f is the fracture energy, L is the characteristic length of the element. The stiffness degradation of the material can be described by D, which varies from 0 (damage initiation) to 1 (failure) [63]. D can be calculated as follows:

$$D = \frac{1-\exp(\lambda\varepsilon^*)}{1-\exp(\lambda)}, \quad \varepsilon^* = \frac{\bar{\varepsilon}^{pl} - \bar{\varepsilon}_0^{pl}}{\bar{\varepsilon}_f^{pl} - \bar{\varepsilon}_0^{pl}} \tag{14}$$

where λ is a coefficient to control the material degradation rate, $\bar{\varepsilon}_0^{pl}$ is the equivalent plastic strain at damage initiation, and $\bar{\varepsilon}_f^{pl}$ is the equivalent plastic strain at failure. G_f and λ are equal to 18.5 kJ/m^2 and 9.4, respectively [20]. Therefore, the stress at the damage stage is calculated by the following equation:

$$\tilde{\sigma} = (1-D)\bar{\sigma} \tag{15}$$

The proposed constitutive model including both plasticity and damage parts is implemented into Abaqus/Explicit through a

VUHARD subroutine using FORTRAN language. It is worth noting that the maximum value of parameter D is limited to be 0.99 because the element deletion cannot occur in the CEL cutting model.

2.4. Johnson-Cook constitutive model

To evaluate the accuracy of the proposed constitutive model in modeling the cutting process, J-C [64] model (plasticity and damage) is also used in orthogonal cutting simulations using CEL approach. This model describes the material flow stress (equation (16)) and plastic strain at damage initiation (equation (17)) as a function of the strain, strain rate, stress triaxiality and temperature. The corresponding equations are represented as follows:

$$\overline{\sigma} = \left(A_{J-C} + B_{J-C}\varepsilon^{n_{J-C}}\right)\left(1 + C_{J-C}ln\left(\frac{\dot{\varepsilon}}{\dot{\varepsilon}_0}\right)\right)\left[1 - \left(\frac{T - T_0}{T_m - T_0}\right)^{m_{J-C}}\right] \tag{16}$$

$$\varepsilon_0^{pl} = \left[D_{1J-C} + D_{2J-C}\exp\left(D_{3J-C}\frac{\sigma_p}{\overline{\sigma}}\right)\right]\left[1 + D_{4J-C}\ln\left(\frac{\dot{\varepsilon}}{\dot{\varepsilon}_0}\right)\right]\left[1 + D_{5J-C}\frac{T - T_r}{T_m - T_r}\right] \tag{17}$$

where: $\overline{\sigma}$ is the equivalent stress; ε_0^{pl} is the equivalent plastic strain at damage initiation; ε and $\dot{\varepsilon}$ are the equivalent plastic strain and strain rate, respectively; T is the temperature; η is the stress triaxiality; $\dot{\varepsilon}_0$ is the reference strain rate; T_r and T_m are the room and melting temperatures, respectively. $A_{J\text{-}C}$, $B_{J\text{-}C}$, $n_{J\text{-}C}$, $m_{J\text{-}C}$, and $C_{J\text{-}C}$ are the coefficients of the J-C plasticity model, while $D_{1J\text{-}C} \sim D_{5J\text{-}C}$ are the coefficients of J-C damage initiation model. The values of these coefficients for the Ti6Al4V titanium alloy are shown in Table 4. The equations of the damage evolution and the related coefficients (G_f and λ) are the same of the above proposed constitutive model (from equation (13) to equation (15)). They are determined by Cheng et al. [20] using the same data used to determine the coefficients of the proposed damage model.

3. Experimental setup

The orthogonal cutting tests were carried out using a five-axis milling center (model DMG MORI DMU 50). The cutting conditions are the same of the orthogonal cutting simulations, including the tool geometry and tool material. The thickness and length of the workpiece are 3 mm (width of cut) and 20 mm (see Fig. 7), respectively. Up milling operation using a milling cutter with 80 mm of diameter. Four values of the cutting speed were used: 50, 125, 250 and 500 m/min. A constant feed per tooth of 0.1 mm/z is used in all the tests. Uncoated cemented carbide inserts are installed in the milling cutter, providing a tool geometry already presented in Section 2.1 (2.2). Tool geometry in the tool-in-hand system according to the ISO standard 3002-1:1982/AMD 1:1992 was carefully inspected using an Alicona InfiniteFocusSL microscope. Several inserts were placed in the milling cuter to measure the tool rake angle, γ_n, tool clearance angle, α_n, and cutting edge radius, r_n. Their values are the following: $\gamma_n = 0 \pm 0.30^o$, $\alpha_n = 15 \pm 0.23^o$, and $r_n = 10 \pm 1.2$ μm. To ensure that tool wear does not affect the results, the total cutting length was very short, and a new tool cutting edge is used at each test. Cutting forces are measured using a Kistler dynamometer, model 9265B. Samples containing several chips are prepared for observing at the optical microscope to measure their geometry (peak, valley and spacing shown in Fig. 24). All samples are prepared by grinding, polishing, and etching with 1 ml HF + 6 ml HNO_3 + 193 ml H_2O solution and observed under an optical microscope. A complete description of the experimental setup is presented by Xu et al. [19].

4. Results and discussion

4.1. Influence of geometry of the CEL element on the results

In this section, simulations using the proposed constitutive model and the CEL approach (the CEL1 model) are conducted to determine the influence of the geometry of the finite element (the element size and its orientation/shape) on the results. This step is essential to determine a suitable element geometry for further CEL simulations.

4.1.1. Influence of the CEL element size on the results

Due to the existence of Eulerian elements with the void in the Eulerian approach, the same computational space requires more elements when compared to the Lagrangian one, which takes more computing time for every incremental step. Besides, it can be deduced from Eq. 13 that the plastic strain at damage evolution depends on the characteristic length of the element, L. So, a decrease of the element size can lead to an unexpected increase of plastic strain. Therefore, the key point is the determination of the element size

Table 4
Coefficients of the Johnson-Cook constitutive model for Ti6Al4V taken from the work of Cheng et al [20].

Coefficient	$A_{J\text{-}C}$ (MPa)	$B_{J\text{-}C}$ (MPa)	$n_{J\text{-}C}$	$m_{J\text{-}C}$	$C_{J\text{-}C}$	$D_{1J\text{-}C}$	$D_{2J\text{-}C}$	$D_{3J\text{-}C}$	$D_{4J\text{-}C}$	$D_{5J\text{-}C}$
Value	812	844	0.261	1.0	0.015	0.245	0.081	-1.276	-0.028	3.87

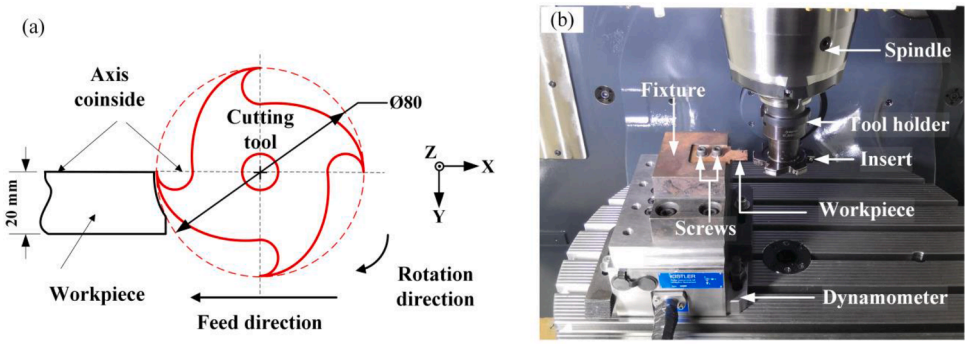

Fig. 7. (a) Schematic representation of the orthogonal cutting tests and (b) corresponding experimental setup.

which ensures an accurate prediction without significantly penalize the calculation efficiency.

A square element is used, and the element size are varied from 10 μm to 2.5 μm. The simulated chip morphology and equivalent plastic strain distribution with different element sizes are presented in Fig. 8.

As shown in Fig. 8a, when the element size is 10 μm, the chip morphology is almost continuous, while experimentally the chips are serrated as shown in Fig. 23*i*. When the element size is reduced to 5 μm (Fig. 8b), the chip morphology becomes serrated, but its geometry is still far from that observed experimentally. Only when the element size is reduced to 3.5 μm (Fig. 8d), the serrated chip morphology becomes close to the experimentally obtained geometry. To quantitatively investigate the influence of the element size on the simulated chip geometry, the chip geometry parameters (peak, valley and spacing) obtained by CEL simulation for several element sizes and experimentally are shown in Fig. 9. The differences between CEL simulations with different element size and experimentally are presented in Table 5.

From Fig. 9 and Table 5, it can be deduced that when the element size decreases from 4 μm to 3.5 μm, the difference between simulated and experimental chip geometry reduces from: 20.5% to 12.8% for the peak; 41% to 37% for the valley; and 28.8% to 18% for the spacing. Further reduction of the element size to 3 μm (Fig. 8e) and even further to 2.5 μm (Fig. 8f) does not improve the simulation results, since it does not affect the chip geometry significantly, and the plastic strain in the shear band unreasonable increases.

The predicted cutting force vs. time is plotted in Fig. 10 for different element sizes. This figure puts in evidence the influence of the cyclic nature of the chip formation in the forces. These forces are not constant, but they vary cyclically along the chip formation process [65].

When the element size is 10 μm, the evolution of cutting force is not smooth, which is very different from that obtained using

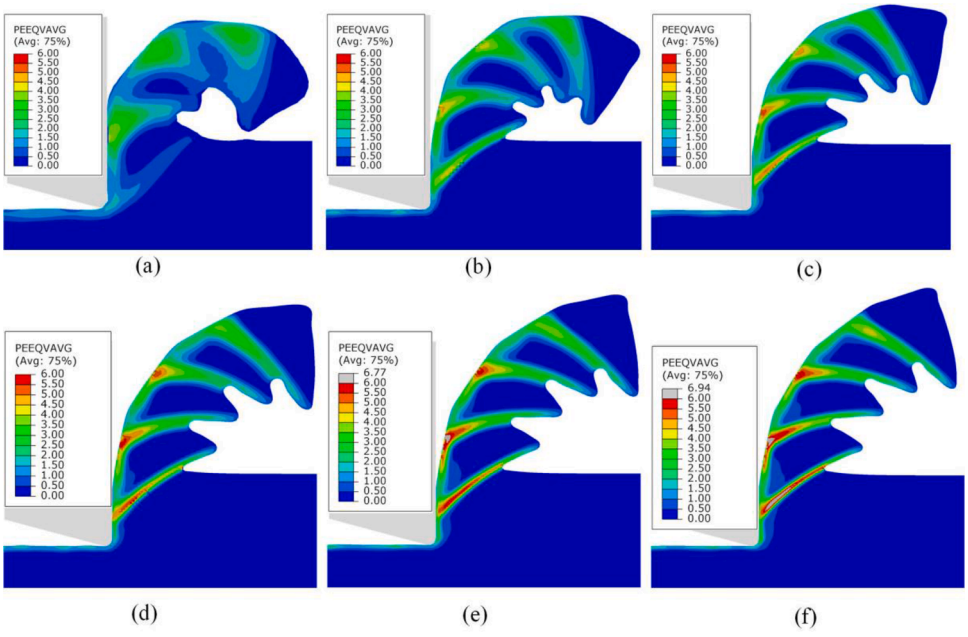

Fig. 8. Chip morphology and distribution of the equivalent plastic strain (PEEQVAVG) obtained using CEL approach with element size of (a) 10 μm, (b) 5 μm, (c) 4 μm, (d) 3.5 μm, (e) 3 μm and (f) 2.5 μm (cutting speed of 250 m/min).

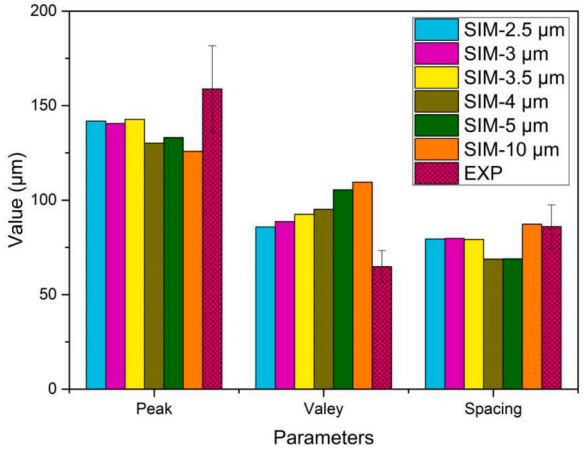

Fig. 9. Chip geometry obtained by CEL simulations for several element sizes and experimentally (cutting speed of 250 m/min).

Table 5
Differences in chip geometry between CEL simulations with different element size and experimentally (cutting speed of 250 m/min).

Element size	10 µm			5 µm			4 µm		
Difference	Peak	Valley	Spacing	Peak	Valley	Spacing	Peak	Valley	Spacing
	23.2%	62.2%	9.7%	18.7%	56.3%	28.6%	20.5%	41%	28.8%
Element size	3.5 µm			3 µm			2.5 µm		
Difference	Peak	Valley	Spacing	Peak	Valley	Spacing	Peak	Valley	Spacing
	12.8%	37%	18%	14.1%	31.4%	17.4%	13.4%	27.1%	17.8%

smaller element sizes. However, cutting force does not change when the element size is less than or equal to 5 µm. It can be deduced that the element size of 5 µm for the CEL simulations is small enough to accurately predict the cutting force. Based on this analysis of the chip morphology and cutting force, the element size of 3.5 µm is selected for the CEL simulations in this study, which allows a balance between calculation accuracy and efficiency.

4.1.2. Influence of the CEL element shape/orientation on the results

The element orientation along the direction of the deformation in FDZ is used in several FE simulations of cutting to facilitate the formation of serrated chips, and to reduce element distortion when using the Lagrangian approach [57,66]. Therefore, it is important to determine the suitable element shape/orientation to be used in the FE simulation of cutting using the CEL approach.

To determine the element shape/orientation, the angle between two adjacent edges of the element is used, as shown in Fig. 11. This figure shows the chip morphology and the equivalent plastic strain distribution for the cutting speed of 250 m/min for three angles of

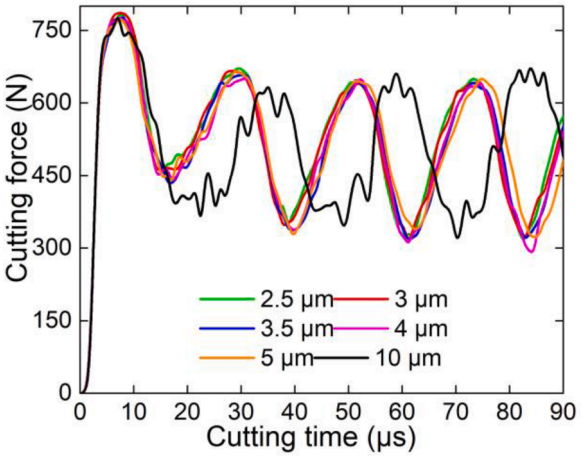

Fig. 10. Cutting force in function of the time for different element size used in CEL simulations.

elements namely 90°, 60°, and 45°. When the element orientation angle is changed from 90° to 60° and then to 45°, the plastic strain in the chip increases significantly, reaching extremely high values. These phenomena are related to the uniqueness of the CEL approach, in which the plastic strain is calculated based on the Eulerian Volume Fraction (EVF). In addition, according to the Abaqus user's manual [50] the contact between the Lagrangian region and the Eulerian need to be smooth. In the current simulations using the tool rake angle of 0°, when the element orientation angle is 60° or 45°, the contact between Eulerian and Lagrangian components appears as point contact and acute angle contact, which will cause the calculation distortion of EVF and an abrupt change during the calculation of the plastic strain. In the CEL simulation, the selection of element shape/orientation depends on the boundary conditions and contact geometry. Therefore, elements with an orientation angle of 90° are used in CEL simulations of orthogonal cutting of Ti6Al4V using a tool rake angle of 0°.

4.1.3. Verification of plane strain conditions for CEL1 model

CEL1 model was developed based on the assumption of plane strain conditions, which need to be verified. The distributions of plastic strain and stress components over the X, Y and Z axes are shown in Fig. 12. As can be seen in Fig. 12 (a), (b) and (c), the plastic strain over the X and Y axes in deformation zone ranges from -1 to 1, while the plastic strain over the Z axis in this zone is approximately zero. Fig. 12 (d), (e) and (f) show that the stress exists over the X, Y and Z axes, especially over the Z axis. This confirms that the 3D CEL1 model is in a plane strain conditions, thus its results can be compared with those obtained by the 2D LAG model, also under plane strain conditions.

4.2. State of stress and strain at damage initiation at the beginning of a chip formation cycle

According to the proposed constitutive model Eqs. (8) and ((15)), the state of stress affects the flow stress and the strain at damage initiation of the work material, and consequently the chip formation, forces, surface integrity and so on. In this section, both the CEL1 and LAG cutting models are used to analyze the state of stress in FDZ at the beginning of a chip formation cycle, and how the cutting speed affects this state.

Considering the CEL1 model, Fig. 13 shows the distributions of the stress triaxiality (Fig. 13a) and Lode parameter (Fig. 13b) in the workpiece and chip, for a cutting speed of 50 m/min. Fig. 14 shows the evolution of the stress triaxiality (Fig. 14a) and Lode parameter (Fig. 14b) along the shear band in FDZ represented in Fig. 13 (path from point 1 to point 10), for several cutting speeds. It follows from Fig. 14a that the values of stress triaxiality along the shear band in FDZ increases from negative near the cutting edge (point 1) to positive at the chip free surface (point 10). This means that, according to Fig. 6, the strain at damage initiation decrease from the tool cutting edge (point 1) to the chip free surface (point 10). This figure also shows that increasing the cutting speed from 50 m/min to 500 m/min, the stress triaxiality becomes less negative near the tool cutting edge, and more positive in the chip free surface. This means that the strain at damage initiation will decrease with the increase of the cutting speed, so less energy is required to remove a layer or material from the workpiece to form the chip [67].

As far as the Lode parameter is concerned, Fig. 14b shows that the Lode parameter increases from zero near the tool cutting edge, to a maximum value of about 0.6-0.8 at the chip free surface. The influence of the cutting speed on the Lode parameter is not so evident as the stress triaxiality. Three zones can be identified along the path from point 1 to point 10: near the cutting edge, in the middle of FDZ, and near the chip free surface. In the zone near the cutting edge, there are no evident influence of the cutting speed on the Lode parameter. Moreover, independently of the cutting speed, the Lode parameter is zero at the chip root. In the middle of FDZ, the Lode parameter decrease as the cutting speed increases. Finally, the Lode parameter increases with the cutting speed near the chip free surface.

According to Fig. 6, the increase of the Lode parameter from zero to both negative and positive ranges leads to an increase of the strain at damage initiation. So, near the tool tip where the Lode parameter is zero, the strain at damage initiation will be lower than that at the chip free surface, where the Lode parameter is maximum.

Fig. 15 and Fig. 16 show the distributions of the state of stress (stress triaxiality and Lode parameter) (Fig. 15), and the evolution of this state of stress along the shear band (Fig. 16), obtained using the LAG model for the same conditions as used in the CEL1 model. These figures show that the stress triaxiality is mainly negative in FDZ, and its magnitude reduces when moving to the chip free surface

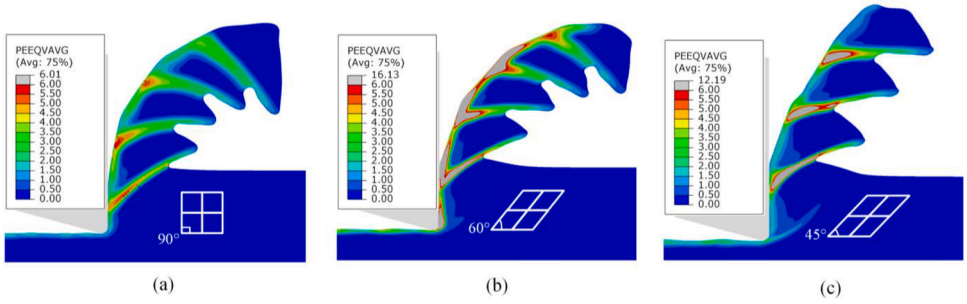

Fig. 11. Chip morphology and distribution of the equivalent plastic strain (PEEQVAVG) obtained using CEL approach with the element angle of (a) 90°, (b) 60°, and (c) 45° (cutting speed of 250 m/min).

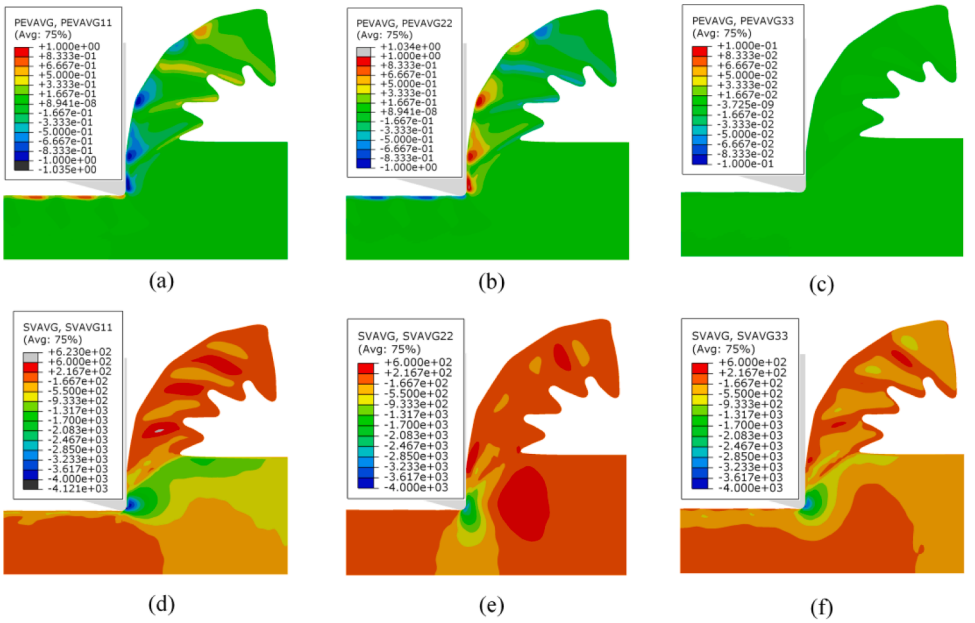

Fig. 12. Plastic strain components ((a) X-axis, (b) Y-axis, and (c) Z-axis) and stress components((d) X-axis, (e) Y-axis, and (f) Z-axis) obtained using CEL1 approach (the cutting speed of 250 m/min).

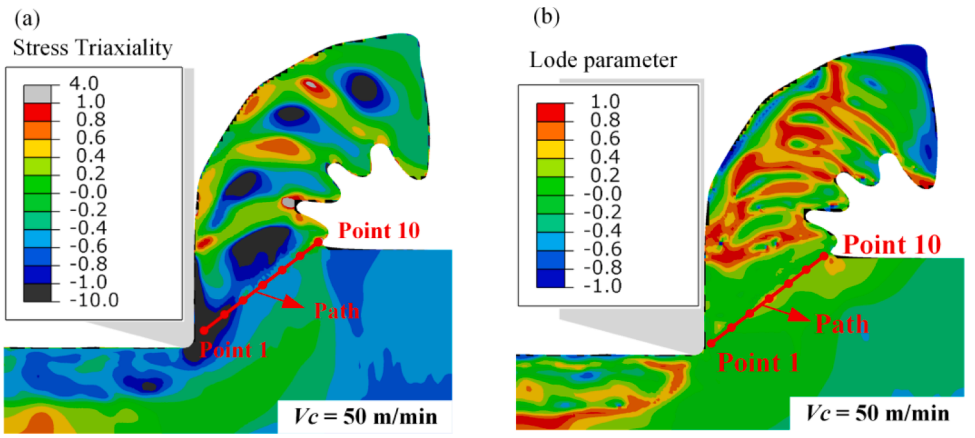

Fig. 13. Distribution of (a) stress triaxiality and (b) Lode parameter, obtained using CEL1 model for a cutting speed of 50 m/min.

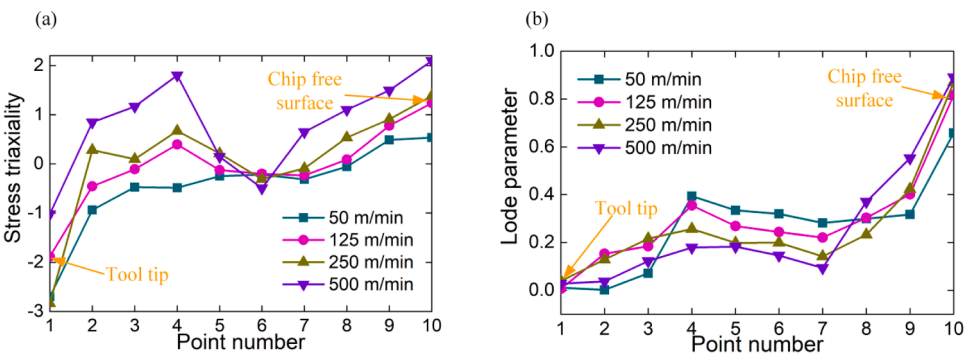

Fig. 14. Evolution of the (a) stress triaxiality and (b) Lode parameter, along the path shows in Fig. 13, obtained using CEL1 model for several cutting speeds (50, 125, 250 and 500 m/min).

(Fig. 15a and Fig. 16a). Moreover, its magnitude is lower than that obtained using the CEL1 model, and there is no evident influence of the cutting speed on the stress triaxiality. This negative stress triaxiality in FDZ is associated with the compressive state of the material at the beginning of the chip formation cycle [31–33]. As far the Lode parameter is concerned, since plane strain conditions are applied in the LAG model, this parameter is almost zero in FDZ (Fig. 16b), while it increases from the cutting edge to the chip free surface in the case when the CEL1 model is used (Fig. 14b).

The strain at damage initiation depends on both stress triaxiality and Lode parameter, as well as on the temperature and strain rate (equation (12)). Fig. 17 and Fig. 18 show the distribution of the strain at damage initiation for the cutting speed of 50 m/min (Fig. 17a and Fig. 18a), and the evolution of the strain at damage initiation along the shear band in FDZ (Fig. 17b and Fig. 18b) for several cutting speeds using both CEL1 and LAG models. As can be seen, the values of the strain at damage initiation decreases from chip free surface to near the tool tip, regardless the cutting speed value. However, this decrease, and the magnitude of the strain at damage initiation are lower when the LAG model is used compared to the results of the CEL1 model. This implies that less energy is required to separate the material from the workpiece to form the chip according to the LAG model, although the same input physical data was used in both models. This is probably due to the different numerical approaches used to simulate the separation of the material from the workpiece.

4.3. Comparison between the Lagrangian and CEL approaches

Simulations using the proposed constitutive model and CEL approach (CEL1 model) are performed, and the results are compared with those obtained using the Lagrangian approach (LAG model). The previous section compares the state of stress and strain at damage initiation obtained using the CEL approach with the Lagrangian one. To complete this analyses, other more practical machining outcomes should also be compared, including the chip geometry, tool-chip contact length, strain, temperature, and forces.

The simulated chip shape and morphologies using both the CEL (CEL1 model) and Lagrangian (LAG model) approaches are shown in Fig. 20a and Fig. 20b, respectively. Both approaches generate similar chip morphologies but predict different tool-chip contact lengths (0.086 mm for the CEL1 model and 0.176 mm for the LAG model). Fig. 19 shows the simulated tool-chip contact length using CEL1 and LAG models in function of the cutting speed and compares with the tool-chip contact length calculated by Poletica equation [68]. This equation is proposed by Poletica [68] after analyzing the tool-chip contact length for a wide range of work materials and cutting conditions, as it is represented by:

$$l_c = h_1 \cdot \zeta^{k_t}$$

where ζ is the chip compression ratio, h_1 is the uncut chip thickness and $k_t = 1.5$ when $\zeta < 4$, and $k_t = 1.3$ when $\zeta \geq 4$.

As shown in this figure, the tool-chip contact length in function of the cutting speed obtained by CEL model have the same trend as the tool-chip contact length calculated by Poletica equation. Moreover, when comparing to the LAG model, the tool-chip contact length obtained by CEL model is closer to that calculated by Poletica equation. Since both CEL1 and LAG models used the same input physical data, this is probably due to the different numerical approaches used to simulate the separation of the material from the workpiece.

Fig. 20 also shows that many distorted elements are generated near the machined surface and in the chip shear band when the Lagrangian approach is used. This does not happen when the CEL approach is used.

The distributions of the equivalent plastic strain and temperature in cutting of Ti6Al4V alloy, obtained using the CEL and Lagrangian approaches, are shown in Fig. 21. As can be seen in Fig. 21a and Fig. 21b, the CEL approach generates the equivalent plastic strain distribution in the shear band of the chips that gradually decreases from the tool cutting edge zone to the chip free surface, while this distribution is relatively uniform when the Lagrangian approach is used. It can be seen in Fig. 21b that the plastic strain of the

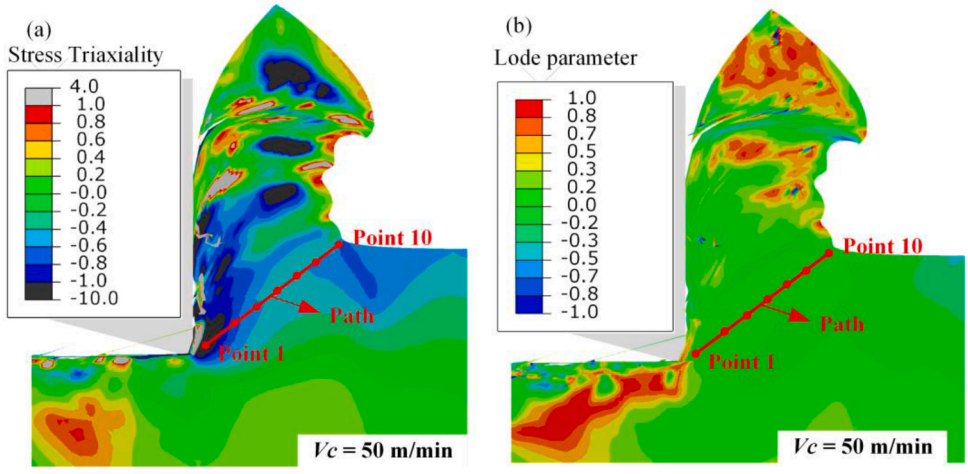

Fig. 15. Distribution of (a) stress triaxiality and (b) Lode parameter, obtained using LAG model for a cutting speed of 50 m/min.

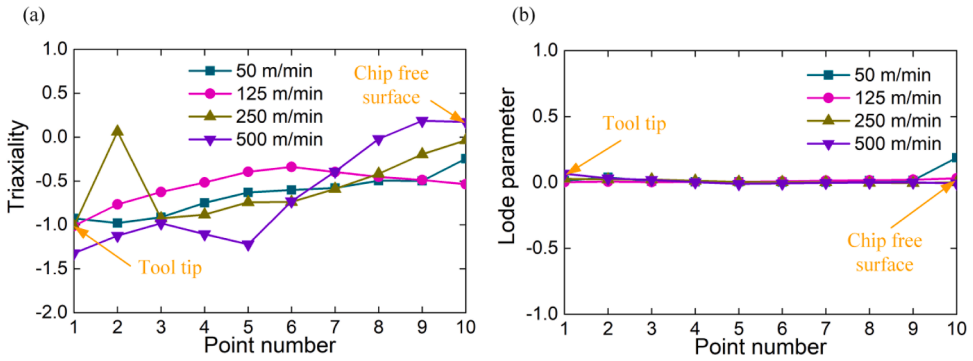

Fig. 16. Evolution of the (a) stress triaxiality and (b) Lode parameter, along the path shows in Fig. 15, obtained using LAG model for several cutting speeds (50, 125, 250 and 500 m/min).

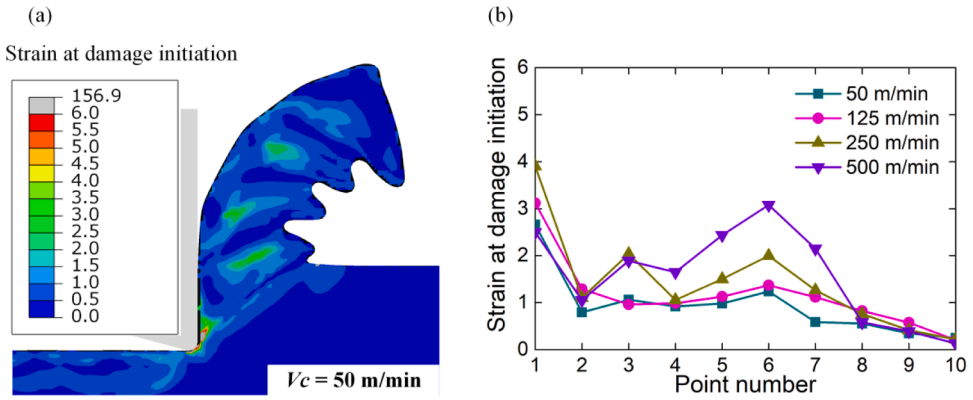

Fig. 17. (a) Distribution of the strain at damage initiation for a cutting speed of 50 m/min, and (b) evolution of the strain at damage initiation along the path shows in Fig. 13, obtained using CEL1 model for several cutting speeds (50, 125, 250 and 500 m/min).

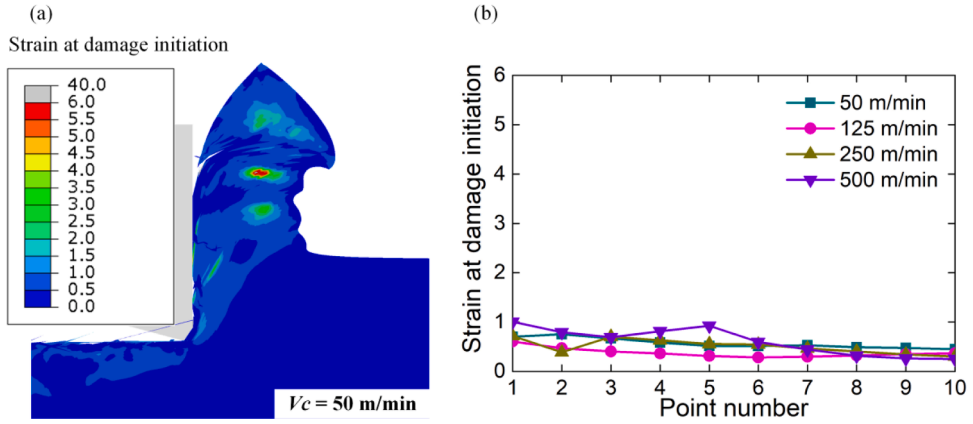

Fig. 18. (a) Distribution of the strain at damage initiation for a cutting speed of 50 m/min, and (b) evolution of the strain at damage initiation along the path shows in Fig. 15, obtained using LAG model for several cutting speeds (50, 125, 250 and 500 m/min).

distorted elements is extremely high, and thus several elements are deleted too early, which has an influence on the final simulated results. Similar results are observed for the temperature distribution, i.e., the CEL approach (Fig. 21c) generates a high localized temperature at the tool-chip interface on the rake face, which is consistent with experimental data [69]. On the contrary, the Lagrangian approach (Fig. 21d) generates a quasi-uniform temperature in the chip over the tool-chip interface, and a high localized temperature in the chip root near the cutting edge. Since the temperature is associated to the thermal energy generated by plastic deformation and friction, the greater plastic strain in the secondary deformation zone compared to other zones obtained by the CEL

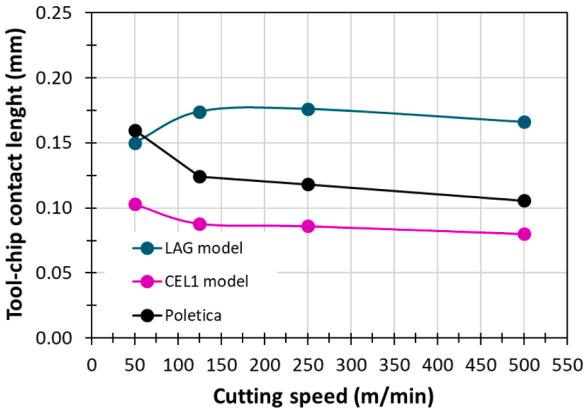

Fig. 19. Simulated tool-chip contact length using CEL1 and LAG models, and comparison with tool-chip contact length calculated by Poletica equation.

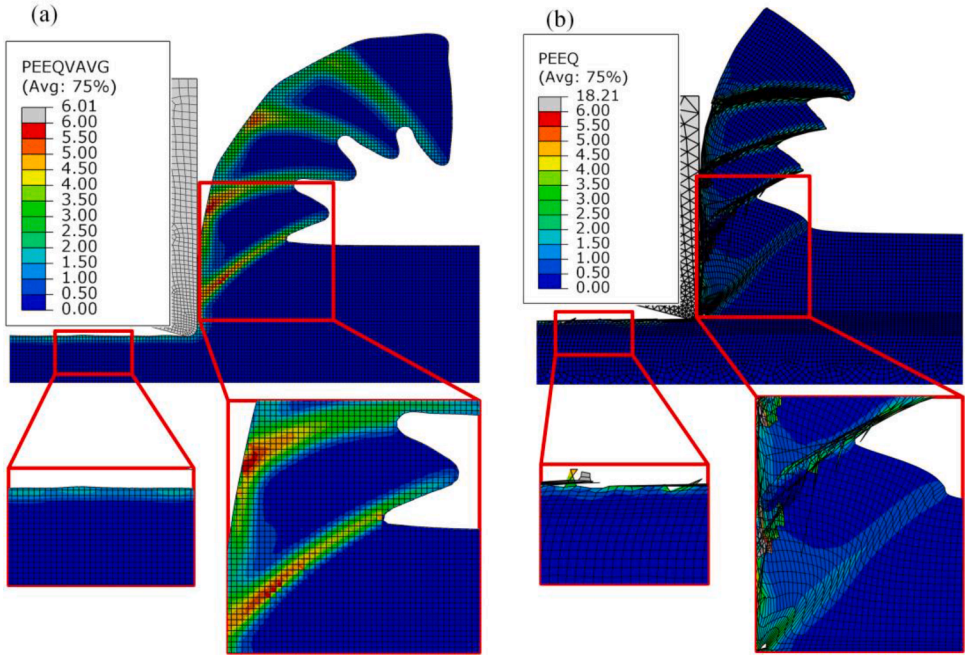

Fig. 20. Chip morphology and distribution of the equivalent plastic strain (PEEQVAVG) obtained using (a) CEL and (b) Lagrangian approaches (cutting speed of 250 m/min).

approach leads to a higher temperature. In Fig. 21d, the temperature in the chip root near the tool cutting edge radius reaches 800°C when the Lagrangian approach is used, but with the deletion of elements in the sacrificial layer, the temperature drops quickly as the deleted elements are no longer involved in the calculation. Besides that, the existence of several elements with extremely high temperatures can lead to a misinterpretation of simulation results.

The cutting forces obtained using both CEL and Lagrangian approaches are plotted in Fig. 22. Both cutting forces vary cyclically in function of the cutting time. However, when the Lagrangian approach is used, this cyclic variation shows small fluctuations, compared to those when CEL approach is used. These fluctuations in the Lagrangian approach are not related to the cutting process itself, but to the element distortion and element deletion in the sacrificed layer.

Element distortion generated by the Lagrangian approach can results in an incorrect calculation of the nodal forces and displacements [7]. Moreover, element deletion (element will no longer participate in the calculation) causes a discontinuity in the calculated stress, strain, and temperature fields. This can significantly affect the predicted results, in particular the surface integrity of the machined surface. This is because the thickness of the layer affected by machining in the workpiece can be shallow (in this work is about 10~25 μm), so that if there are a large number of distorted elements in this thickness, the extraction and interpretation of the results become very difficult. Therefore, the cutting model including the CEL approach combined with the proposed constitutive model

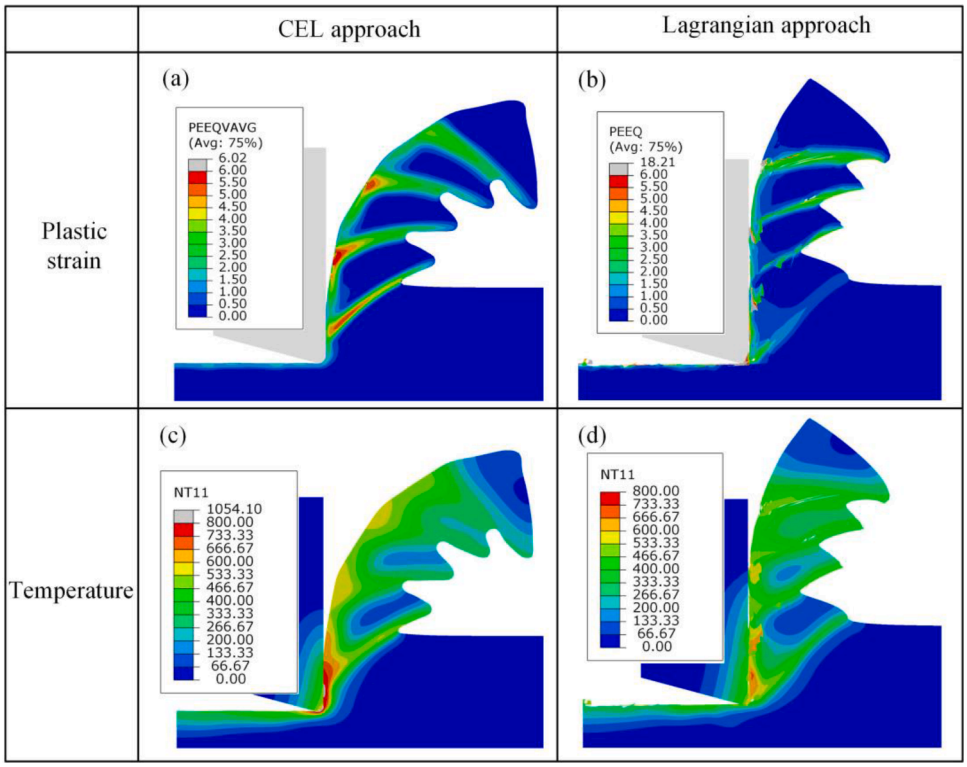

Fig. 21. Distributions of the equivalent plastic strain ((a) and (b)) and temperature ((c) and (d)) obtained using CEL (CEL1 model) ((a) and (c)) and Lagrangian (LAG model) ((b) and (d)) approaches (cutting speed of 250 m/min).

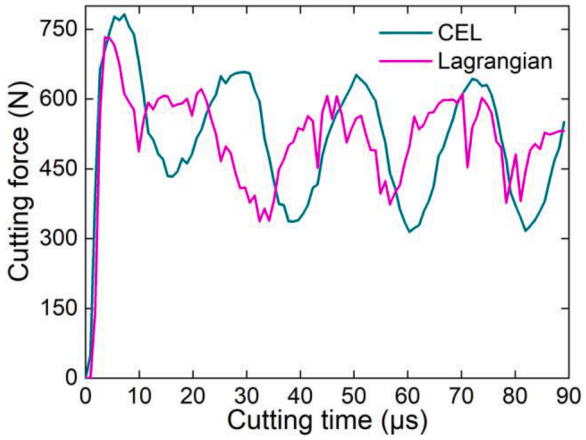

Fig. 22. Cutting force in function of the time obtained by CEL and Lagrangian approaches (cutting speed of 250 m/min).

has great advantages in machining simulation of Ti6Al4V titanium alloy since it avoids element distortion, thus can better predict the serrated chip geometry, forces, and plastic strain.

The durations of the calculations of these three proposed models were obtained for the same cutting conditions, corresponding to the cutting speed of 250 m/min and using the same computation environment. The results show that CEL2 model needed 23.4 hours to complete the simulation, while CEL1 just needed 2.6 hours and LAG – 1.7 hours. Although the CEL2 is closer to the actual cutting process, the long time, and thus high computation cost is the major inconvenient. It is worth noting that the computation cost of CEL2 model can be reduced by decreasing the total number of elements. Thus, a mesh optimization is required to decrease the computation cost without compromising the accuracy of the simulated results. From the computation efficiency perspective, CEL1 model is preferred due to the low computation cost, but it should be used with cautions under the assumption of plane strain condition.

4.4. Comparison between the proposed constitutive model and the Johnson-Cook model

To verify the accuracy of the cutting model using the CEL approach (CEL1) together with the proposed constitutive model, the predicted and measured cutting force and chip morphology are compared for several cutting speeds. Fig. 23 shows the experimental and simulated chip morphology using J-C and the proposed constitutive models obtained varying the cutting speeds from 50 m/min to 500 m/min. The J-C model generates a chip morphology almost continuous, and it does not change significantly with the cutting speed, being quite different from the chip morphology observed experimentally. Shear localization in the chip gradually increases with the cutting speed. Moreover, the serrated chips are observed using the proposed constitutive model, and the chip geometry changes significantly with the cutting speed. It can be deduced from Fig. 23 that the chip morphology predicted by the proposed constitutive model is closer to the experimental one when compared to the chip morphology predicted by the J-C constitutive model. To compare the chip geometry obtained by CEL simulations and experimentally, the geometric characteristics of the serrated chips are presented. The chip peak, valley, and spacing (see Fig. 24) are measured and the obtained results are shown in Fig. 25 and listed in Table 6. It was found that the differences between simulated and experimental values of the peak and spacing are within the range of the experimental error. It can also be seen that the differences between simulated and measured values of the valley are a bit higher, in particular for the cutting speeds of 250 m/min and 500 m/min.

Fig. 26 shows the evolution of the cutting force as a function of time obtained by CEL simulations using both J-C and the proposed constitutive model at the cutting speed of 250 m/min. The amplitude and frequency of the cutting force are related to the cyclic nature of chip formation. As can be seen, the amplitude of the cutting force generated using the J-C constitutive model is smaller than that of the proposed one, while the opposite is true for the frequency. As far as the average cutting force is concerned, the J-C constitutive model generates a higher force compared to the proposed constitutive model and the experimental results (see also Table 7). Moreover, the proposed constitutive model generates an average cutting force close to that obtained experimentally.

Therefore, the proposed constitutive model is more accurate than the J-C model in the prediction of chip geometry and cutting force during HSM of Ti6Al4V alloy. Fig. 27 and Fig. 28 can be used to explain the reasons for the better predictability of the proposed constitutive model. Fig. 27 shows the simulated distributions of the equivalent plastic strain (PEEQVAVG) and von Mises stress (SVAVG) using the CEL approach (CEL1 model), for both the J-C and the proposed constitutive model.

Fig. 28a and Fig. 28b show the von Mises stress as a function of the plastic strain for a tracking point in the middle of the shear band of FDZ (see Fig. 27a and Fig. 27b) obtained using the CEL approach with the J-C model and the proposed constitutive model at the cutting speed of 250 m/min.

In Fig. 28a, the von Mises stress generated by the J-C model is higher than that of the proposed model for the same strain. This is also confirmed by observing the distribution of the von Mises stress in FDZ (Fig. 27c and Fig. 27d). Due to this higher stress, the cutting force generated using the J-C model is higher than that using the proposed model (see Fig. 26). It can be seen in Fig. 28b that the plastic strain at damage initiation using the proposed model is lower than that using the J-C model.

Fig. 29 shows von Mises stress as a function of the plastic strain for a tracking point in the middle of the shear band of FDZ, obtained by CEL approach using the proposed constitutive model at different cutting speeds. As can be seen, the maximum stress increases with the cutting speed due to the combined influence of the strain rate and temperature, and the stress triaxiality. However, the plastic strain at damage initiation decreases with the cutting speed due to the increased stress triaxiality (Fig. 14a) whereas the Lode parameter is zero near the cutting edge where the material is separated from the workpiece to form the chip (Fig. 14b).

4.5. Material flow in the Z-direction (the side flow)

Previously predicted results are obtained using the 3D orthogonal cutting model using the CEL approach having a small width of cut (CEL1). However, this model does not permit to simulate the material side flow often observed experimentally. Therefore, a 3D orthogonal cutting model using the CEL approach with the actual width of cut (CEL2) of 3 mm is also developed, and the obtained results are compared with CEL1. Fig. 30 shows the plastic strain and temperature distributions extracted from: 1) the lateral surface of the workpiece of CEL1 model (designed in Fig. 30 by "CEL1 model"); 2) a plane passing through the middle of the workpiece of the CEL2 model (designed in Fig. 30 by "CEL2 model (middle surface)"); 3) the lateral surface of the workpiece of CEL2 model (designed in Fig. 30 by "CEL2 model (lateral surface)"). A comparison between the results over the middle surface obtained using the CEL1 and CEL2 models (see Fig. 30a, b, c, and d) shows that the strain and temperature have almost the same distributions, which verifies the consistency between the CEL1 and CEL2 models. However, a relatively lower strain and temperature are the case at the lateral surface when the CEL2 is used compared with the results in the middle surface as shown in Fig. 30c and Fig. 30f.

As shown in Fig. 31, the material side flow (the red dotted line area) is found when the CEL2 model is used. This flow occurs in the chip (its width becomes greater than the width of cut) and in the machined surface in the form of side burr. Although the work material is constrained in the Z-direction in the front face (symmetry condition), it is free to move in the opposite side, resulting in an increase of chip width and formation of lateral burrs on the machined surface. The material side flow is observed experimentally in the chip and machined surface using an optical microscope and SEM. Fig. 32 shows the experimental chip free surface for several cutting speeds. Table 8 shows a comparison between simulated and experimental chip width. For the same cutting speed, experimental and simulated values of the chip width are almost same. Depending on the cutting speed, the chips are wider about 50-140 μm than the width of cut (3mm). Fig. 33 shows the lateral burr on the machined surface observed using SEM.

As shown in Fig. 30, the strain distribution over the middle surface is different from that distribution in the lateral surface of the workpiece. This implies that the deformation conditions in the middle section and lateral surface of the workpiece are not the same. Therefore, if plane strain conditions can be assumed in the middle section, this is not the case for the lateral surface. In the testing

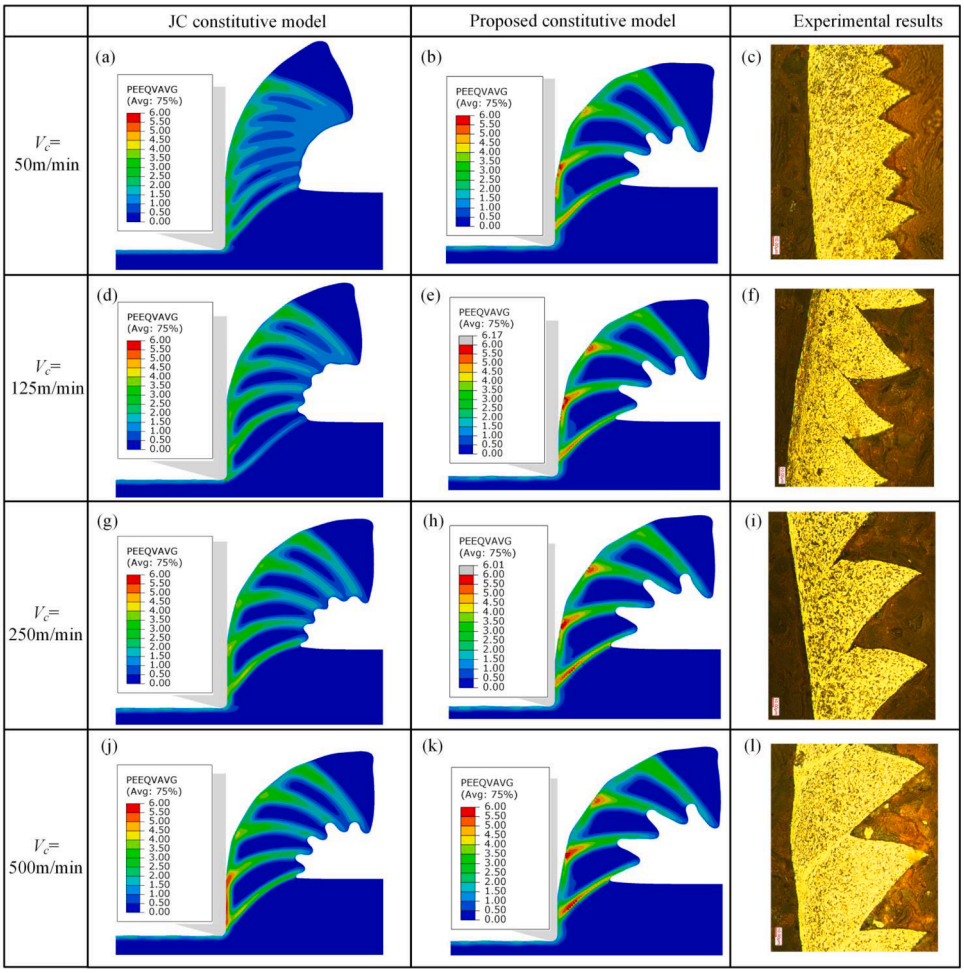

Fig. 23. Simulated chip morphology and distribution of the equivalent plastic strain (PEEQVAVG) obtained using CEL approach, using the Johnson-Cook and the proposed constitutive models at several cutting speeds (50, 125, 250 and 500 m/min). Experimental chip morphology.

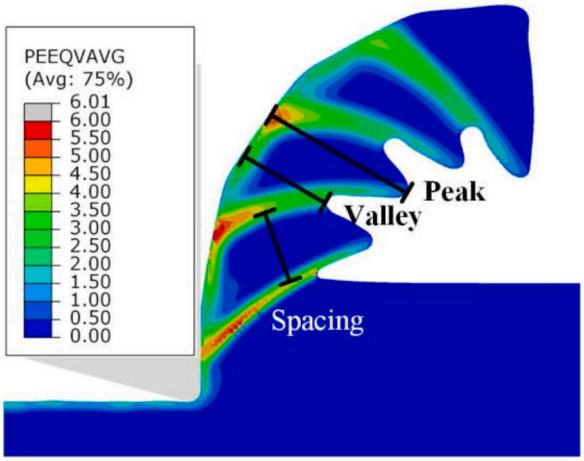

Fig. 24. Distribution of the equivalent plastic strain (PEEQVAVG) and parameters of chip geometry obtained using CEL approach (cutting speed of 250 m/min).

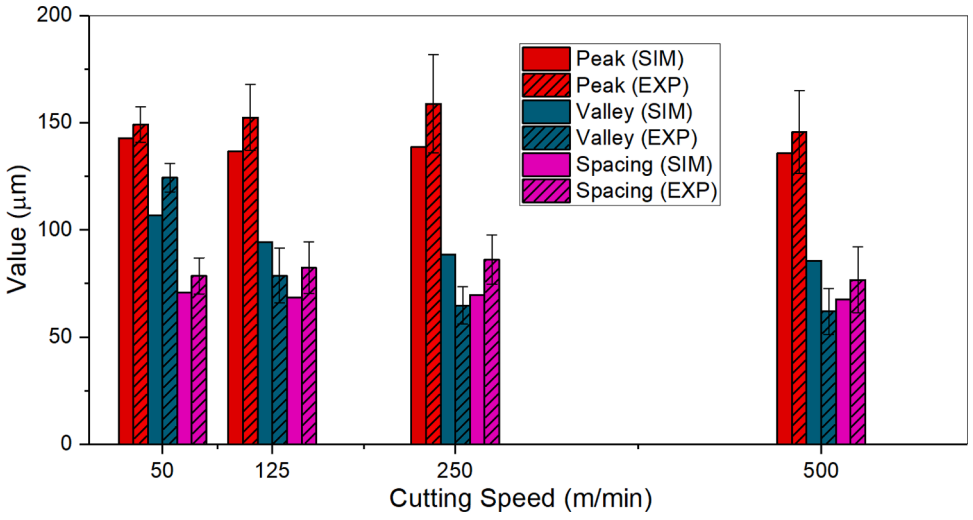

Fig. 25. Chip geometry obtained by CEL simulations and experimentally for several cutting speeds.

Table 6
Chip geometry differences between CEL simulated and experimentally obtained chips for several cutting speeds.

Cutting speed	50 m/min			125 m/min		
Difference	Peak	Valley	Spacing	Peak	Valley	Spacing
	4.3%	14.2%	9.8%	10.4%	20%	16.8%
Cutting speed	250m/min			500m/min		
Difference	Peak	Valley	Spacing	Peak	Valley	Spacing
	12.7%	36.6%	19.1%	6.7%	38.3%	12%

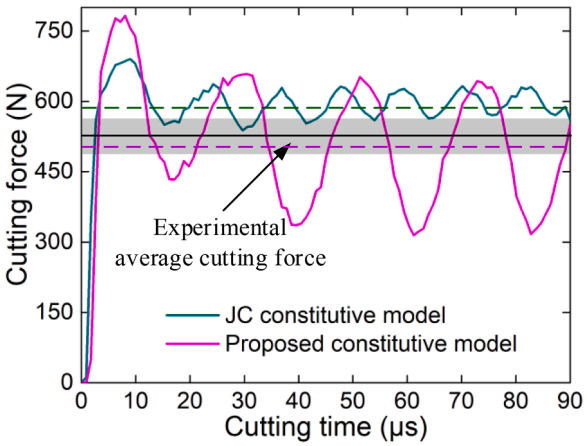

Fig. 26. Simulated cutting force as a function of the time obtained using both J-C (green) and the proposed (magenta) constitutive model (cutting speed of 250 m/min), and the comparison with the average cutting force (black line with gray region indicating the standard deviation).

Table 7
Comparison between simulated and experimental cutting force.

Cutting Speed (m/min)	Simulated force F_t (N) Average	Experimental force F_t (N) Average	Difference (%)
50 m/min	519.5	541.4±20.9	4%
125 m/min	505.1	523.2±25.3	3.5%
250 m/min	493.8	512.1±24.7	3.6%
500 m/min	474.2	480.6±32.1	1.2%

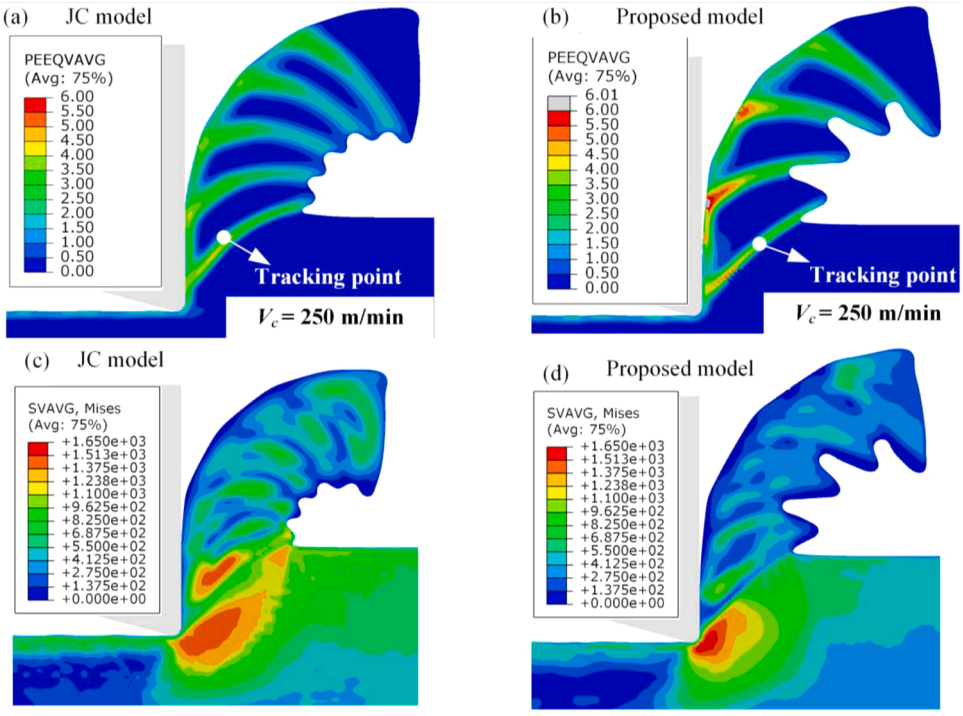

Fig. 27. Results of CEL simulations: (a) Plastic strain distribution using J-C constitutive model, (b) plastic strain distribution using the proposed constitutive model, (c) von Mises stress distribution using J-C constitutive model, (d) von Mises stress distribution using the proposed constitutive model.

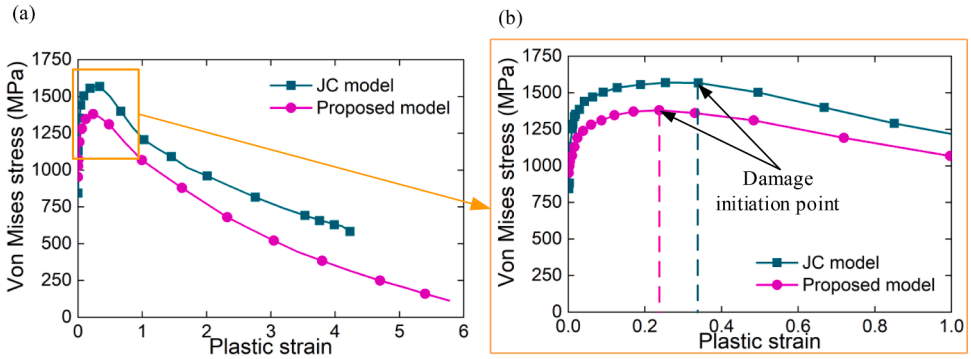

Fig. 28. von Mises stress in function of the plastic strain for a tracking point in the middle of the shear band of FDZ shown in Fig. 27, for the J-C and the proposed constitutive models, respectively (the cutting speed of 250 m/min).

practice, the temperature distribution during cutting is often obtained by thermal cameras and the strain distribution by high speed imaging cameras using the Digital Image Correlation (DIC) technique [70]. Both temperature and strain distributions are obtained only for the lateral surface of the workpiece and chip, whereas numerical simulation allows to assess temperatures and strains over the whole width of the workpiece and chip. Therefore, 3D cutting models need to be developed to correctly compare the simulated strain distribution with that obtained experimentally by DIC. The same is applied when comparing the simulated temperature distribution and that measured by thermal cameras. Unfortunately, this is not taken into account in many known publications [71–73].

4.6. Cyclic variation of the plastic strain and surface topography

The CEL2 model is used to analyze the influence of the cyclic nature of the chip formation on the plastic strain at the machined surface and the surface topography along the cutting direction, although the same analysis could be done using CEL1 model. Fig. 34 shows the plastic strain distribution in the machined surface for several cutting speeds. The same as for the cutting force (Fig. 10 and Fig. 22), a cyclic variation of the plastic strain in the cutting direction is obtained. This cyclic variation is due to the changes of the state

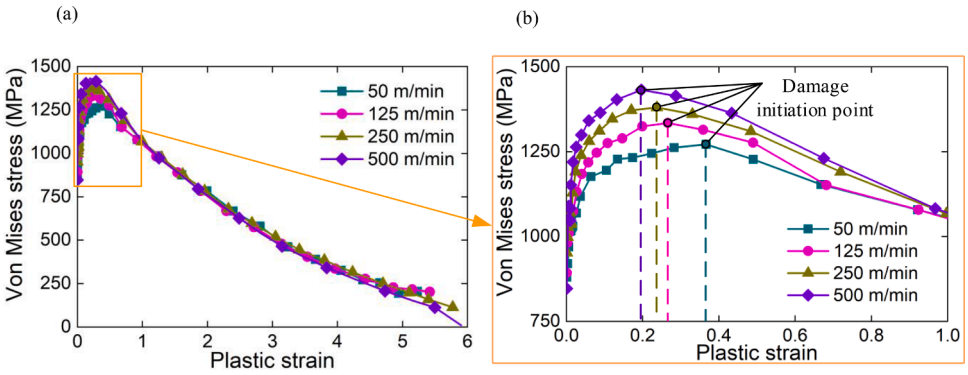

Fig. 29. von Mises stress vs. of the plastic strain using the proposed constitutive model in CEL simulations at different cutting speeds (50, 125, 250 and 500 m/min).

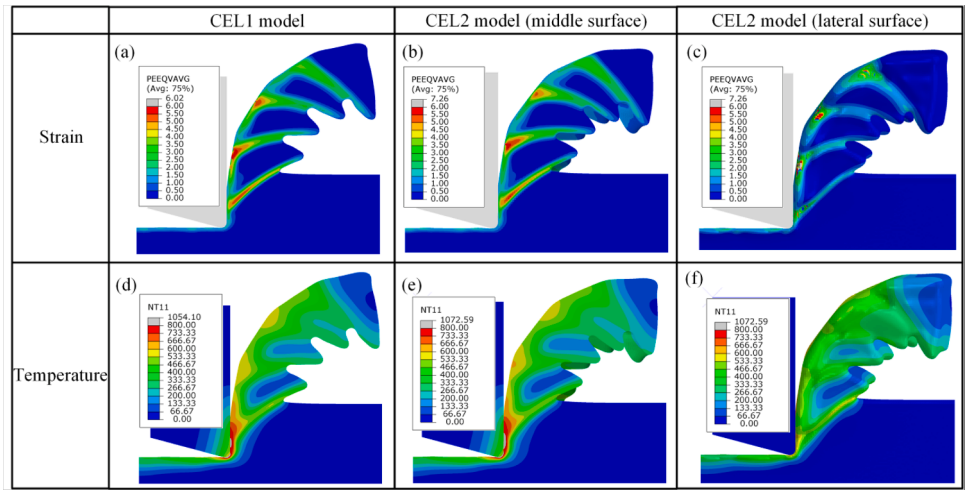

Fig. 30. Distributions of the plastic strain and temperature using the CEL1 ((a) and (d)) and CEL2 ((b), (c), (e) and (f)) models. Distributions are obtained in a plane passing through the middle of the workpiece of the CEL2 model and at the lateral surface of the workpiece of both CEL1 and CEL2 models. The cutting speed is constant and equal to 250 m/min.

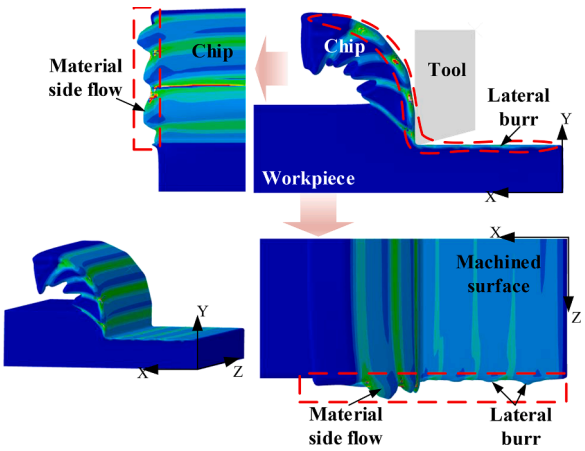

Fig. 31. Several projection views of serrated chip morphology and machined surface simulated using the CEL2 model at the cutting speed of 250 m/min. This figure put in evidence the formation of lateral burr in the machined surface and the increased chip width compared to the width of cut.

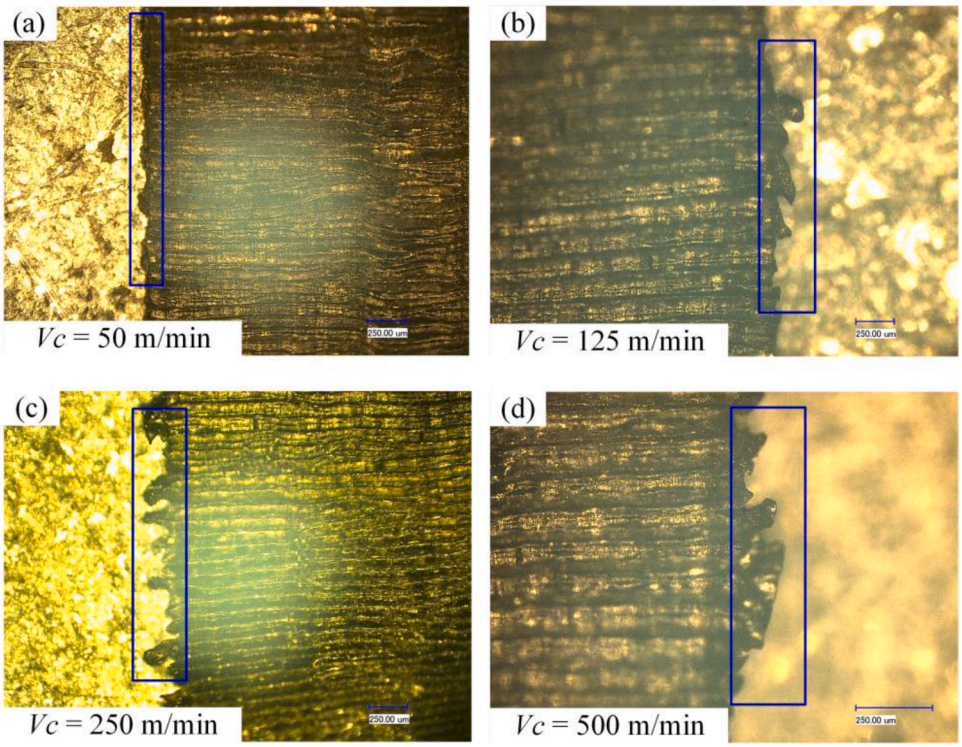

Fig. 32. Experimental chip free surface for several cutting speeds, observed at the optical microscope.

Table 8
Comparison between simulated and experimental chip width.

Cutting Speed (m/min)	Simulated (SIM) Average	Maximum	Experimental (EXP) Average	Maximum	Difference between EXP and SIM (average) (%)	Difference between EXP chip width and the width of cut (average) (mm)
50 m/min	3.06±0.02	3.08	3.05±0.02	3.08	0.33%	0.05
125 m/min	3.08±0.02	3.10	3.08±0.03	3.12	0%	0.08
250 m/min	3.09±0.03	3.12	3.14±0.05	3.19	1.62%	0.14
500 m/min	3.10±0.03	3.13	3.13±0.07	3.21	0.97%	0.13

of stress, and consequently localization of the strain in the shear bands. Fig. 35 shows both simulated and experimental topography of the machined surface for several cutting speeds: 125, 250 and 500 m/min. As can be seen, the surface topography varies cyclically in the cutting direction. Moreover, the measured total height of the roughness profile (R_t) obtained by the white light interferometer and the simulated profile of the surface topography in the cutting direction are very similar in terms of amplitude and period for the highest cutting speed of 500 m/min, and slightly different for the other speeds of 125 and 250 m/min. These results show the influence of the cyclic nature of chip formation in machining Ti6Al4V on the plastic strain and surface roughness. However, other parameters of the surface integrity are also affected, including the microstructure and the residual stresses [74]. This will be investigated in detail in future research works.

5. Conclusions

Models of HSM of Ti6Al4V alloy are developed and simulated using both the Lagrangian and CEL approaches, including the proposed constitutive model considering the state of stress in addition of the strain, strain rate, and temperature. A sensitivity analysis of the mesh topography on the chip geometry and cutting force permitted to determine a maximum element size of 3.5 μm and an element orientation of 90° to be used in CEL simulations. Compared with the traditional Lagrangian approach, the CEL approach has outstanding advantages by avoiding the element distortion, which is important for simulating HSM. In addition, the following conclusions can be drawn:

1 Cutting model using the CEL approach and the proposed constitutive model allow to simulate serrated chips in machining Ti6Al4V alloy for a wide range of cutting speeds, ranging from 50 m/min to 500 m/min.
2 CEL approach can better predict the strains and tool-chip contact length than the Lagrangian one.

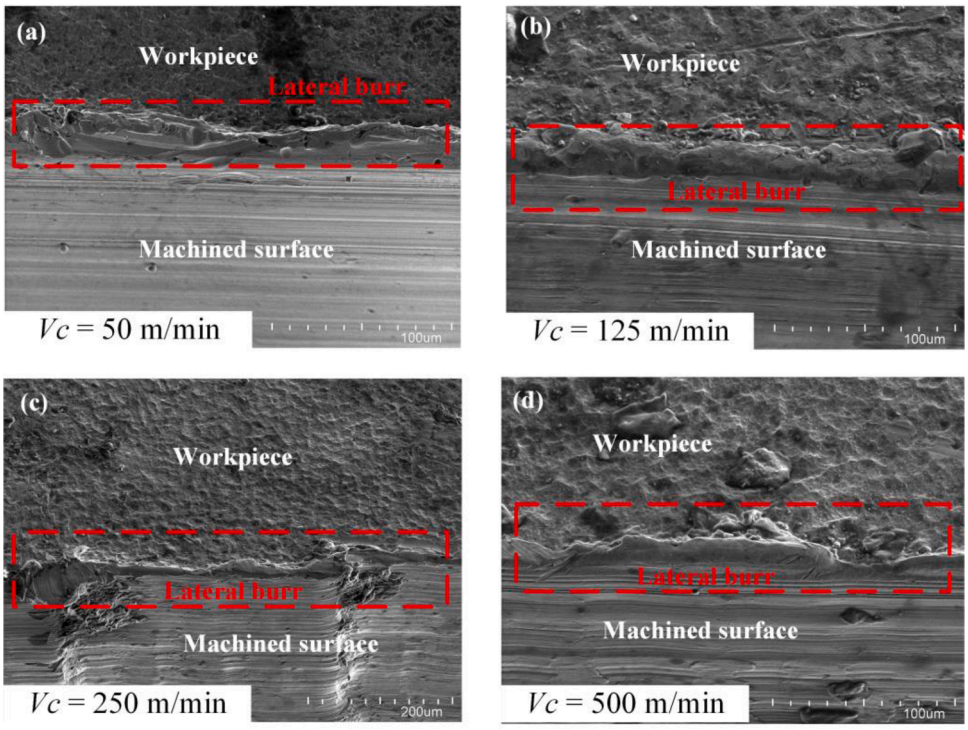

Fig. 33. SEM images of the lateral burr in the workpiece for several cutting speeds.

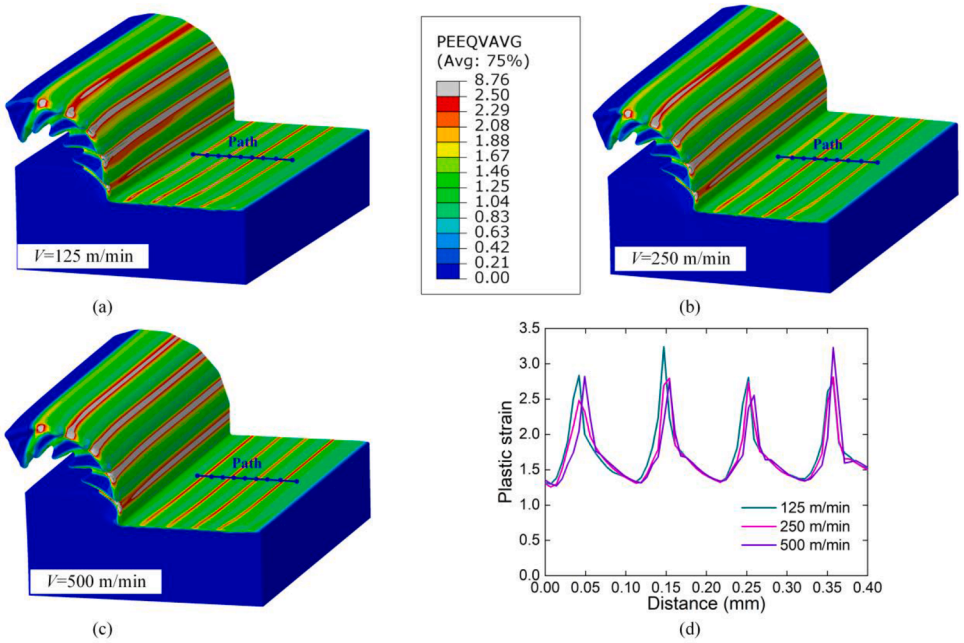

Fig. 34. Distribution of the plastic strain (PEEQVAVG) obtained by CEL simulation for a cutting speed of (a) 125 m/min, (b) 125 m/min, (c) 500 m/min; (d) plastic strain profiles at the machined surface along the cutting direction, for several cutting speeds.

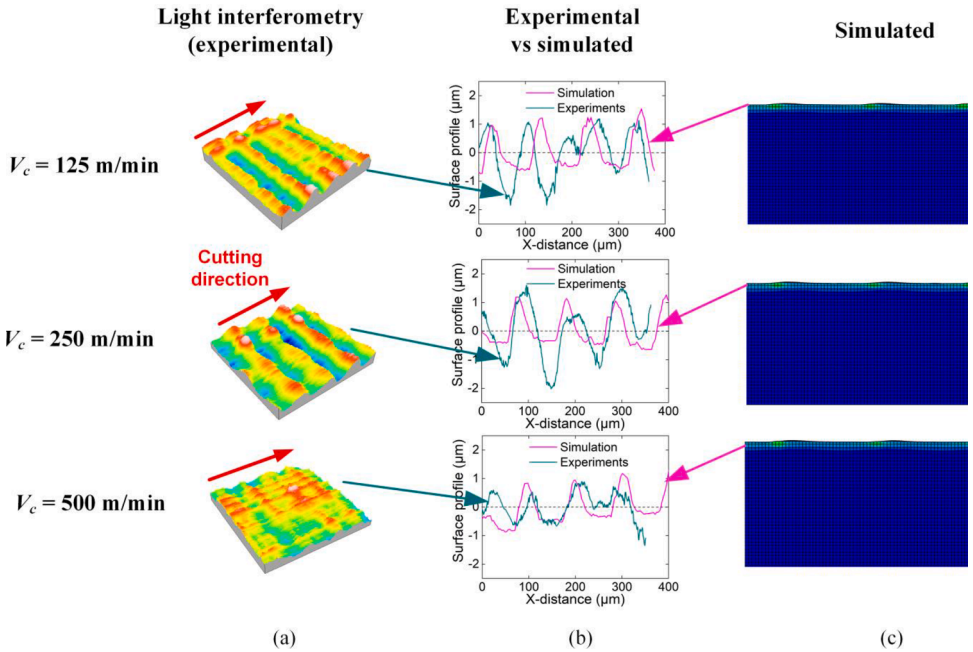

Fig. 35. (a) Measured surface topography obtained by white light interferometry (R_t parameter), (b) comparison between simulated and measured profiles, and (c) simulation surface topography obtained by CEL simulations (cutting speeds: 125, 250 and 500 m/min).

3 Increasing the cutting speed increases the maximum stress and decreases the strain at damage initiation. This is due to the increase of the strain rate and the decrease of the stress triaxiality when the cutting speed increases.
4 The proposed constitutive model predicts the cutting force and chip geometry much closer to experimental results than J-C model, because it provides a more realistic thermomechanical behavior of the Ti6Al4V alloy in cutting.
5 CEL simulations using larger width of cut permitted to simulate the material side flow, which results in a larger width of chip when compared to the width of cut, and the formation of lateral burr in the workpiece This implies that the plane strain conditions often assumed in 2D simulations of orthogonal cutting cannot accurately represent the reality.
6 The CEL-based model allows to simulate the cyclic variation of the plastic strain and topography of the machined surface along the cutting direction, observed experimentally. Because of this, the other important parameters of the surface integrity (e.g. residual stress, microstructure, and microhardness) also have the same cyclic variation. This capability of the CEL-based models provides a completely new perspective for simulations of surface integrity, when significantly affects the performance of the machined parts in critical applications [75]. This new ability with a great practical significance is achieved when the proper model of the work material behavior in cutting is used.

Declarations of Competing Interest

None

Acknowledgment

This work is supported by the National Natural Science Foundation of China (Grant No. 51675417) and the Shaanxi Science Foundation for Distinguished Young Scholars [2019J-C08]. The author would also like to acknowledge financial support from the China Scholarship Council (NO.201906280422). The authors would like to thank Dr. Lamice Denguir from Arts et Metiers Institute of Technology for her valuable advice in developing the CEL approach and modeling. They would like also to thank Mr. Baochen Li and Dr. Hongguang Liu from Xi'an Jiaotong University for their help in the HSM experiments and SEM observation.

References

[1] T. Thepsonthi, T. Özel, Experimental and finite element simulation based investigations on micro-milling Ti-6Al-4V titanium alloy: Effects of cBN coating on tool wear, J. Mater. Process. Technol. 213 (2013) 532–542, https://doi.org/10.1016/j.jmatprotec.2012.11.003.
[2] B. Wang, Z. Liu, Q. Yang, Investigations of yield stress, fracture toughness, and energy distribution in high speed orthogonal cutting, Int. J. Mach. Tools Manuf. 73 (2013) 1–8, https://doi.org/10.1016/j.ijmachtools.2013.05.007.
[3] L.A. Denguir, J.C. Outeiro, G. Fromentin, V. Vignal, R. Besnard, A physical-based constitutive model for surface integrity prediction in machining of OFHC copper, J. Mater. Process. Technol. (2017) 248, https://doi.org/10.1016/j.jmatprotec.2017.05.009.

[4] R. Liu, S. Melkote, R. Pucha, J. Morehouse, X. Man, T. Marusich, An enhanced constitutive material model for machining of Ti-6Al-4V alloy, J. Mater. Process. Technol. 213 (2013) 2238–2246, https://doi.org/10.1016/j.jmatprotec.2013.06.015.
[5] Y. Zhang, J.C. Outeiro, T. Mabrouki, On the selection of Johnson-Cook constitutive model parameters for Ti-6Al-4V using three types of numerical models of orthogonal cutting, Procedia CIRP 31 (2015) 112–117, https://doi.org/10.1016/j.procir.2015.03.052.
[6] P.J. Arrazola, T. Özel, D. Umbrello, M. Davies, I.S. Jawahir, Recent advances in modelling of metal machining processes, CIRP Ann. - Manuf. Technol. 62 (2013) 695–718, https://doi.org/10.1016/j.cirp.2013.05.006.
[7] T. Mabrouki, C. Courbon, Y. Zhang, J. Rech, D. Nélias, M. Asad, H. Hamdi, S. Belhadi, F. Salvatore, Some insights on the modelling of chip formation and its morphology during metal cutting operations, Comptes Rendus - Mec 344 (2016) 335–354, https://doi.org/10.1016/j.crme.2016.02.003.
[8] S.N. Melkote, W. Grzesik, J. Outeiro, J. Rech, V. Schulze, H. Attia, P.J. Arrazola, R. M'Saoubi, C. Saldana, Advances in material and friction data for modelling of metal machining, CIRP Ann. - Manuf. Technol. 66 (2017) 731–754, https://doi.org/10.1016/j.cirp.2017.05.002.
[9] M. Röthlin, H. Klippel, M. Afrasiabi, K. Wegener, Metal cutting simulations using smoothed particle hydrodynamics on the GPU, Int. J. Adv. Manuf. Technol. 102 (2019) 3445–3457, https://doi.org/10.1007/s00170-019-03410-0.
[10] Y. He, J. Zhang, Y. Qi, H. Liu, A.R. Memon, W. Zhao, Numerical study of microstructural effects on chip formation in high speed cutting of ductile iron with discrete element method, J. Mater. Process. Technol. 249 (2017) 291–301, https://doi.org/10.1016/j.jmatprotec.2017.06.006.
[11] G. Oger, S. Marrone, D.Le Touzé, M. de Leffe, SPH accuracy improvement through the combination of a quasi-Lagrangian shifting transport velocity and consistent ALE formalisms, J. Comput. Phys. 313 (2016) 76–98, https://doi.org/10.1016/j.jcp.2016.02.039.
[12] Y. Bai, T. Wierzbicki, A new model of metal plasticity and fracture with pressure and Lode dependence, Int. J. Plast. 24 (2008) 1071–1096, https://doi.org/10.1016/j.ijplas.2007.09.004.
[13] M.N.A. Nasr, E.G. Ng, M.A. Elbestawi, Modelling the effects of tool-edge radius on residual stresses when orthogonal cutting AISI 316L, Int. J. Mach. Tools Manuf. 47 (2007) 401–411, https://doi.org/10.1016/j.ijmachtools.2006.03.004.
[14] Y. Avevor, J. Vincent, L. Faure, A. Moufki, S. Philippon, An ALE approach for the chip formation process in high speed machining with transient cutting conditions: Modeling and experimental validation, Int. J. Mech. Sci. 130 (2017) 546–557, https://doi.org/10.1016/j.ijmecsci.2017.06.021.
[15] F. Ducobu, E. Rivière-Lorphèvre, E. Filippi, Application of the Coupled Eulerian-Lagrangian (CEL) method to the modeling of orthogonal cutting, Eur. J. Mech. A/Solids. 59 (2016) 58–66, https://doi.org/10.1016/j.euromechsol.2016.03.008.
[16] F. Ducobu, E. Rivière-Lorphèvre, E. Filippi, Mesh influence in orthogonal cutting modelling with the Coupled Eulerian-Lagrangian (CEL) method, Eur. J. Mech. A/Solids. 65 (2017) 324–335, https://doi.org/10.1016/j.euromechsol.2017.05.007.
[17] F. Ducobu, P.J. Arrazola, E. Rivière-Lorphèvre, G.O. De Zarate, A. Madariaga, E. Filippi, The CEL Method as an Alternative to the Current Modelling Approaches for Ti6Al4V Orthogonal Cutting Simulation, Procedia CIRP 58 (2017) 245–250, https://doi.org/10.1016/j.procir.2017.03.188.
[18] F. Shuang, X. Chen, W. Ma, Numerical analysis of chip formation mechanisms in orthogonal cutting of Ti6Al4V alloy based on a CEL model, Int. J. Mater. Form. 11 (2018) 185–198, https://doi.org/10.1007/s12289-017-1341-z.
[19] X. Xu, J. Zhang, J. Outeiro, B. Xu, W. Zhao, Multiscale simulation of grain refinement induced by dynamic recrystallization of Ti6Al4V alloy during high speed machining, J. Mater. Process. Technol. 286 (2020), 116834, https://doi.org/10.1016/j.jmatprotec.2020.116834.
[20] W. Cheng, J. Outeiro, J.P. Costes, R. M'Saoubi, H. Karaouni, V. Astakhov, A constitutive model for Ti6Al4V considering the state of stress and strain rate effects, Mech. Mater. 137 (2019), 103103, https://doi.org/10.1016/j.mechmat.2019.103103.
[21] G.R. Johnson, W.H. Cook, A constitutive model and data from metals subjected to large strains, high strain rates and high temperatures, in: Proc. 7th Int. Symp. Ballist. Hague, Netherlands, 1983, pp. 541–547.
[22] F. Ducobu, P.-J. Arrazola, E. Rivière-Lorphèvre, E. Filippi, On the selection of an empirical material constitutive model for the finite element modeling of Ti6Al4V orthogonal cutting, including the segmented chip formation, Int. J. Mater. Form. (2020), https://doi.org/10.1007/s12289-020-01535-2.
[23] B. Wang, Z. Liu, Shear localization sensitivity analysis for Johnson-Cook constitutive parameters on serrated chips in high speed machining of Ti6Al4V, Simul. Model. Pract. Theory. 55 (2015) 63–76, https://doi.org/10.1016/j.simpat.2015.03.011.
[24] M. Calamaz, D. Coupard, F. Girot, A new material model for 2D numerical simulation of serrated chip formation when machining titanium alloy Ti-6Al-4V, Int. J. Mach. Tools Manuf. 48 (2008) 275–288, https://doi.org/10.1016/j.ijmachtools.2007.10.014.
[25] M. Sima, T. Özel, Modified material constitutive models for serrated chip formation simulations and experimental validation in machining of titanium alloy Ti-6Al-4V, Int. J. Mach. Tools Manuf. 50 (2010) 943–960, https://doi.org/10.1016/j.ijmachtools.2010.08.004.
[26] D. Umbrello, S. Rizzuti, J.C. Outeiro, R. Shivpuri, Modeling of the flow stress for AISI H13 tool steel during hard machining processes, in: AIP Conf. Proc., 2007.
[27] M. Sadeghifar, M. Javidikia, V. Songmene, M. Jahazi, Finite element simulation-based predictive regression modeling and optimum solution for grain size in machining of Ti6Al4V alloy: Influence of tool geometry and cutting conditions, Simul. Model. Pract. Theory. 104 (2020), 102141, https://doi.org/10.1016/j.simpat.2020.102141.
[28] Y. Estrin, H.S. Kim, Modelling microstructure evolution toward ultrafine crystallinity produced by severe plastic deformation, J. Mater. Sci. 42 (2007) 1512–1516, https://doi.org/10.1007/s10853-006-1282-2.
[29] H. Ding, N. Shen, Y.C. Shin, Modeling of grain refinement in aluminum and copper subjected to cutting, Comput. Mater. Sci. 50 (2011) 3016–3025, https://doi.org/10.1016/j.commatsci.2011.05.020.
[30] S. Imbrogno, S. Rinaldi, D. Umbrello, L. Filice, R. Franchi, A. Del Prete, A physically based constitutive model for predicting the surface integrity in machining of Waspaloy, Mater. Des. 152 (2018) 140–155, https://doi.org/10.1016/j.matdes.2018.04.069.
[31] J. Time, Mémoire sur le rabotage des métaux, Expédition pour la confection des papiers de l'Etat, 1877. Petersbourg, Russia.
[32] J.T. Nicolson, Experiments with a Lathe-Tool Dynamometer, Proc. Inst. Mech. Eng. 67 (1904) 883–935, https://doi.org/10.1243/PIME_PROC_1904_067_018_02.
[33] F.W. Taylor, On the art of cutting metals, Trans. ASME. 28 (1907) 70–350.
[34] M. Okoshi, S. Fucui, Researches on the cutting action of planning tool by micokinematographic, photoelastic and piezoelectric methods, Sci. Pap. Inst. Phys. Chem. Res. 22 (1933) 97–166.
[35] H. Liu, J. Zhang, X. Xu, W. Zhao, Experimental study on fracture mechanism transformation in chip segmentation of Ti-6Al-4V alloys during high-speed machining, J. Mater. Process. Technol. 257 (2018) 132–140, https://doi.org/10.1016/j.jmatprotec.2018.02.040.
[36] X. Zhang, R. Shivpuri, A.K. Srivastava, Chip fracture behavior in the high speed machining of titanium alloys, J. Manuf. Sci. Eng. Trans. ASME. 138 (2016) 1–14, https://doi.org/10.1115/1.4032583.
[37] B. Wang, Z. Liu, Evaluation on fracture locus of serrated chip generation with stress triaxiality in high speed machining of Ti6Al4V, Mater. Des. 98 (2016) 68–78, https://doi.org/10.1016/j.matdes.2016.03.012.
[38] T.H.C. Childs, P.J. Arrazola, P. Aristimuno, A. Garay, I. Sacristan, Ti6Al4V metal cutting chip formation experiments and modelling over a wide range of cutting speeds, J. Mater. Process. Technol. 255 (2018) 898–913, https://doi.org/10.1016/j.jmatprotec.2018.01.026.
[39] Y. Bai, T. Wierzbicki, Application of extended Mohr-Coulomb criterion to ductile fracture, Int. J. Fract. 161 (2010) 1–20, https://doi.org/10.1007/s10704-009-9422-8.
[40] B. Wang, X. Xiao, V.P. Astakhov, Z. Liu, The effects of stress triaxiality and strain rate on the fracture strain of Ti6Al4V, Eng. Fract. Mech. 219 (2019), 106627, https://doi.org/10.1016/j.engfracmech.2019.106627.
[41] S. Buchkremer, F. Klocke, D. Veselovac, 3D FEM simulation of chip breakage in metal cutting, Int. J. Adv. Manuf. Technol. 82 (2016) 645–661, https://doi.org/10.1007/s00170-015-7383-9.
[42] Y.M. Arisoy, C. Guo, B. Kaftanoḡlu, T. Özel, Investigations on microstructural changes in machining of Inconel 100 alloy using face turning experiments and 3D finite element simulations, Int. J. Mech. Sci. 107 (2016) 80–92, https://doi.org/10.1016/j.ijmecsci.2016.01.009.
[43] D. Umbrello, A. Bordin, S. Imbrogno, S. Bruschi, 3D finite element modelling of surface modification in dry and cryogenic machining of EBM Ti6Al4V alloy, CIRP J. Manuf. Sci. Technol. 18 (2017) 92–100, https://doi.org/10.1016/j.cirpj.2016.10.004.

[44] A. Yıldız, A. Kurt, S. Yağmur, Finite element simulation of drilling operation and theoretical analysis of drill stresses with the deform-3D, Simul. Model. Pract. Theory. 104 (2020), 102153, https://doi.org/10.1016/j.simpat.2020.102153.
[45] A. Attanasio, E. Ceretti, J. Outeiro, G. Poulachon, Numerical simulation of tool wear in drilling Inconel 718 under flood and cryogenic cooling conditions, Wear 458–459 (2020), 203403, https://doi.org/10.1016/j.wear.2020.203403.
[46] N. Ying, J. Feng, Z. Bo, A novel 3D finite element simulation method for longitudinal-torsional ultrasonic-assisted milling, Int. J. Adv. Manuf. Technol. 106 (2020) 385–400, https://doi.org/10.1007/s00170-019-04636-8.
[47] G. Liu, C. Huang, R. Su, T. Özel, Y. Liu, L. Xu, 3D FEM simulation of the turning process of stainless steel 17-4PH with differently texturized cutting tools, Int. J. Mech. Sci. 155 (2019) 417–429, https://doi.org/10.1016/j.ijmecsci.2019.03.016.
[48] J.C. Outeiro, J.C. Pina, R. M'Saoubi, F. Pusavec, I.S. Jawahir, Analysis of residual stresses induced by dry turning of difficult-to-machine materials, CIRP Ann. - Manuf. Technol. 57 (2008), https://doi.org/10.1016/j.cirp.2008.03.076.
[49] X. Xu, J. Zhang, H. Liu, Y. Qi, Z. Liu, W. Zhao, Effect of morphological evolution of serrated chips on surface formation during high speed cutting Ti6Al4V, Procedia CIRP 77 (2018) 147–150, https://doi.org/10.1016/j.procir.2018.08.262.
[50] D.S.C. Simulia, Abaqus Analysis User's Manual, 2016. http://www.maths.cam.ac.uk/computing/software/abaqus_docs/docs/v6.12/pdf_books/BENCHMARKS.pdf.
[51] L.C. da Silva, P.R. da Mota, M.B. da Silva, E.O. Ezugwu, Á.R. Machado, Study of burr behavior in face milling of PH 13-8 Mo stainless steel, CIRP J. Manuf. Sci. Technol. 8 (2015) 34–42, https://doi.org/10.1016/j.cirpj.2014.10.003.
[52] T. Régnier, G. Fromentin, B. Marcon, J. Outeiro, A. D'Acunto, A. Crolet, T. Grunder, Fundamental study of exit burr formation mechanisms during orthogonal cutting of AlSi aluminium alloy, J. Mater. Process. Technol. 257 (2018) 112–122, https://doi.org/10.1016/j.jmatprotec.2018.02.037.
[53] R. Liu, E. Eaton, M. Yu, J. Kuang, An Investigation of Side Flow during Chip Formation in Orthogonal, Procedia Manuf 10 (2017) 568–577, https://doi.org/10.1016/j.promfg.2017.07.053.
[54] V. Pednekar, V. Madhavan, A.H. Adibi-Sedeh, Investigation of the transition from plane strain to plane stress in orthogonal metal cutting, in: ASME 2004 Int. Mech. Eng. Congr. Expo. 255, 2004, pp. 513–528, https://doi.org/10.1115/IMECE2004-62167.
[55] T. Özel, M. Sima, A.K. Srivastava, B. Kaftanoglu, Investigations on the effects of multi-layered coated inserts in machining Ti-6Al-4V alloy with experiments and finite element simulations, CIRP Ann. - Manuf. Technol. 59 (2010) 77–82, https://doi.org/10.1016/j.cirp.2010.03.055.
[56] G. Chen, C. Ren, X. Yang, X. Jin, T. Guo, Finite element simulation of high-speed machining of titanium alloy (Ti-6Al-4V) based on ductile failure model, Int. J. Adv. Manuf. Technol. 56 (2011) 1027–1038, https://doi.org/10.1007/s00170-011-3233-6.
[57] Y. Zhang, T. Mabrouki, D. Nelias, Y. Gong, FE-model for Titanium alloy (Ti-6Al-4V) cutting based on the identification of limiting shear stress at tool-chip interface, Int. J. Mater. Form. 4 (2011) 11–23, https://doi.org/10.1007/s12289-010-0986-7.
[58] N.N. Zorev, Interrelationship between shear processes occurring along tool face and on shear plane in metal cutting, Roceedings Int. Res. Prod. Eng. Conf. (1963) 42–49.
[59] C. Courbon, F. Pusavec, F. Dumont, J. Rech, J. Kopac, Influence of cryogenic lubrication on the tribological properties of Ti6Al4V and Inconel 718 alloys under extreme contact conditions, Lubr. Sci. 26 (2014) 315–326, https://doi.org/10.1002/ls.1254.
[60] T. Dos Santos, J.C. Outeiro, R. Rossi, P. Rosa, A New Methodology for Evaluation of Mechanical Properties of Materials at Very High Rates of Loading, Procedia CIRP 58 (2017) 481–486, https://doi.org/10.1016/j.procir.2017.03.258.
[61] D. Yameogo, B. Haddag, H. Makich, M. Nouari, A physical behavior model including dynamic recrystallization and damage mechanisms for cutting process simulation of the titanium alloy Ti-6Al-4V, Int. J. Adv. Manuf. Technol. 100 (2019) 333–347, https://doi.org/10.1007/s00170-018-2663-9.
[62] G.R. Johnson, W.H. Cook, Fracture characteristics of three metals subjected to various strains, strain rates, temperatures and pressures, Eng. Fract. Mech. 21 (1985) 31–48, https://doi.org/10.1016/0013-7944(85)90052-9.
[63] Y.M. Abushawashi, Modeling of metal cutting as purposeful fracture of work material, Michigan State University, 2013.
[64] T.J. Holmquist, G.R. Johnson, A computational constitutive model for glass subjected to large strains, high strain rates and high pressures, J. Appl. Mech. Trans. ASME. 78 (2011) 541–547, https://doi.org/10.1115/1.4004326.
[65] V.P. Astakhov, Metal cutting mechanics, CRC press, 1998.
[66] B. Wang, Z. Liu, Investigations on the chip formation mechanism and shear localization sensitivity of high-speed machining Ti6Al4V, Int. J. Adv. Manuf. Technol. 75 (2014) 1065–1076, https://doi.org/10.1007/s00170-014-6191-y.
[67] V.P. Astakhov, S. Shvets, The assessment of plastic deformation in metal cutting, J. Mater. Process. Technol. 146 (2004) 193–202, https://doi.org/10.1016/j.jmatprotec.2003.10.015.
[68] M.F. Poletica, Contact Loads on Cutting Tool Interface Surfaces, Mashinostroenie, Moscow, 1969.
[69] V.P. Astakhov, J.C. Outeiro, Importance of Temperature in Metal Cutting and Its Proper Measurement/Modeling, in: J.P. Davim (Ed.), Meas. Mach. Tribol., Springer International Publishing, 2019, pp. 1–47, https://doi.org/10.1007/978-3-030-03822-9_1.
[70] B. Pan, K. Qian, H. Xie, A. Asundi, Two-dimensional digital image correlation for in-plane displacement and strain measurement: A review, Meas. Sci. Technol. 20 (2009), https://doi.org/10.1088/0957-0233/20/6/062001.
[71] J.C. Outeiro, S. Campocasso, L.A. Denguir, G. Fromentin, V. Vignal, G. Poulachon, Experimental and numerical assessment of subsurface plastic deformation induced by OFHC copper machining, CIRP Ann. - Manuf. Technol. 64 (2015), https://doi.org/10.1016/j.cirp.2015.04.080.
[72] D. Zhang, X.M. Zhang, H. Ding, Hybrid digital image correlation-finite element modeling approach for modeling of orthogonal cutting process, J. Manuf. Sci. Eng. Trans. ASME. 140 (2018), https://doi.org/10.1115/1.4038998.
[73] D. Zhang, X.M. Zhang, W.J. Xu, H. Ding, Stress Field Analysis in Orthogonal Cutting Process Using Digital Image Correlation Technique, J. Manuf. Sci. Eng. Trans. ASME. 139 (2017), https://doi.org/10.1115/1.4033928.
[74] J.C. Outeiro, F. Rossi, G. Fromentin, G. Poulachon, G. Germain, A.C. Batista, Process mechanics and surface integrity induced by dry and cryogenic machining of AZ31B-O magnesium alloy. Procedia CIRP, 2013, https://doi.org/10.1016/j.procir.2013.06.138.
[75] I.S. Jawahir, E. Brinksmeier, R. M'Saoubi, D.K. Aspinwall, J.C. Outeiro, D. Meyer, D. Umbrello, A.D. Jayal, Surface integrity in material removal processes: Recent advances, CIRP Ann. - Manuf. Technol. 60 (2011), https://doi.org/10.1016/j.cirp.2011.05.002.